

1 **Dynamics of episodic magma injection and migration at**
2 **Yellowstone caldera: revisiting the 2004-2009 episode of**
3 **caldera uplift with InSAR and GPS data**

4 **Francisco Delgado, Raphaël Grandin**

5 ¹Université de Paris, Institut de Physique du Globe de Paris, CNRS, F-75005 Paris, France

6 **Key Points:**

- 7 • We reanalyze all the InSAR and GPS data that span the 2004-2009 episode of
8 unrest
9 • The GPS and InSAR time series record uplift with an exponential increase
10 followed by an exponential decrease indicating magma injection
11 • Magma migration cannot explain subsidence at the Norris Geyser basin

Corresponding author: Francisco Delgado, delgado@ipgp.fr

Abstract

The 2004-2009 caldera uplift is the largest instrumentally recorded episode of unrest at Yellowstone caldera. We use GPS and InSAR time series spanning 2004-2015, with a focus in the aforementioned event to understand the mechanisms of unrest. InSAR data recorded ~ 25 and ~ 20 cm of uplift at the Sour Creek (SCD) and Mallard Lake (MLD) resurgent domes during 2004-2009, and ~ 8 cm of subsidence at the Norris Geyser Basin (NGB) during 2004-2008. The SCD/MLD uplift was followed by subsidence across the caldera floor with a maximum at MLD of ~ 1.5 - 2.5 cm/yr and no deformation at NGB. The best-fit source models for the 2004-2009 period are two horizontal sills at depths of ~ 8.7 and 10.6 km for the caldera source and NGB, respectively, with volume changes of 0.354 and -0.121 km³, and an overpressure of ~ 0.1 MPa. The InSAR and GPS time series record exponentially increasing followed by exponentially decreasing uplift between 2004 and 2009, which is indicative of magma injection into the caldera reservoir, with no need for other mechanisms. However, magma extraction from NGB to the caldera is unable to explain the subsidence coeval with the caldera uplift. Models of magma injection can also explain other episodes of caldera uplift like that in 2014-2015. Distributed sill opening models show that magma is stored across the caldera source with no clear boundary between MLD and SCD. Since the magma overpressure is orders of magnitude below the tensile strength of the encasing rock, historical episodes of unrest like these are very unlikely to trigger an eruption.

1 Introduction

Silicic volcanoes ($\text{SiO}_2 > 69\%$) are responsible for the largest explosive eruptions on Earth ($\text{VEI} > 8$, *Miller and Wark (2008)*; *Bachmann and Bergantz (2008)*), more than two orders of magnitude larger than any eruption with recorded visual and instrumental observations. These eruptions form calderas that can remain restless even several hundreds of thousands of years after the climactic eruptions (e.g., *Hill et al. (2020)*). Several of these calderas undergo transient pulses or cycles of ground uplift followed by periods of either quiescence or ground subsidence (*Pelton and Smith, 1979*; *Dvorak and Berrino, 1991*). However, their relation to potential eruptive activity has remained elusive (e.g., *Pritchard et al. (2019)*). The advent of interferometric synthetic aperture radar (InSAR) geodesy in the early 1990s provided the first detailed images of the spatial and temporal complexities of these ground deformation cycles, which have been imaged at Yellowstone (*Wicks et al. (1998, 2006)*; *Chang et al. (2007)*, *Chang et al. (2010)*), Long Valley (*Fialko et al., 2001a*; *Liu et al., 2011*; *Montgomery-Brown et al., 2015*), Campi Flegrei (*Lundgren et al., 2001*; *Trasatti et al., 2015*; *D'Auria et al., 2015*), Santorini (*Parks et al., 2012*), Laguna del Maule (*Feigl et al., 2014*; *Le Mével et al., 2015*), and Cordón Caulle (*Jay et al., 2014*; *Delgado et al., 2016*), (*Delgado et al., 2018*) volcanoes. These uplift events have velocities of ~ 1 - 10 cm/yr, but can reach fast rates up to 28 - 45 cm/yr (*Feigl et al., 2014*; *Delgado et al., 2016*). The spatial and time scales of the deformation events vary from ~ 15 km in Long Valley to more than 70 km at Yellowstone, and from ~ 6 months for Cordón Caulle (*Delgado et al., 2018*) up to at least half a century for Yellowstone (*Pelton and Smith, 1979*). These signals have been interpreted as being produced by either magma injection in shallow reservoirs (*Wicks et al., 2006*; *Delgado et al., 2018*; *Miller et al., 2017*), volatile exsolution (*Dzurisin et al., 2012*; *Hildreth, 2017*), fluid flow in the hydrothermal systems that are located in several of these systems (*Hurwitz et al., 2007a*), viscoelastic relaxation (*Novoa et al., 2019*) or a combination of these processes (*Dzurisin et al., 2012*; *Tizzani et al., 2015*). However, inherent ambiguities in the interpretation of the geodetic data and the lack of other constraining independent data sets like microgravity, gas chemistry, seismology and heat flow measurements have prevented scientists from unraveling the geological mechanism of ground uplift for most of them. Despite the diversity of monitoring data acquired in the past 40 years, recent studies that try to reconcile the wealth of geologic and geophysical data of Long Val-

65 ley (*Hildreth, 2017; Hill et al., 2020*) and Campi Flegrei (*Troise et al., 2019; D’Auria*
66 *et al., 2015*) calderas show no agreement upon the driving mechanism of unrest.

67 Understanding of these unrest signals requires a thorough knowledge of the processes
68 that occur inside these magma reservoirs. For instance, most of the models
69 available for modeling ground deformation data assume injection of fluid magma with
70 Newtonian viscosity into a pressurized cavity (*Lengline et al., 2008; Le Mével et al.,*
71 *2016*). Other models incorporate volatile exsolution instead of magma pressurization
72 resulting in very similar uplift signals compared to those predicted by magma injection
73 models (*Hurwitz et al., 2007a; Hutnak et al., 2009; Todesco et al., 2010*). Viscoelastic
74 models usually do not explicitly take magma injection into account (*Newman et al.,*
75 *2006; Delgado et al., 2018; Novoa et al., 2019*), but as they require a prescribed pressure
76 relaxation function, the driving mechanism is likely magmatic up to the point when viscous
77 relaxation dominates over the instantaneous elastic response. This is in contrast with
78 the current understanding of the plumbing system of silicic volcanoes as crystal mushes,
79 in which reservoirs are not molten but solid sponge-like bodies with pores filled with in-
80 terstitial fluids and melt (*Bachmann and Bergantz, 2008; Bachmann and Huber, 2016;*
81 *Cashman et al., 2017; Cooper, 2017*). These mushes have a protracted growth history
82 by episodic amalgamation of a stack of sill-shaped reservoirs (*Annen, 2009; Annen*
83 *et al., 2015*), and spend most of their lifetime below their solidus under cold storage
84 conditions (*Cooper and Kent, 2014; Rubin et al., 2017*). Crystal mushes are unlikely
85 to produce a volcanic eruption unless they are thermomechanically unlocked and remobilized
86 by many episodic pulses of magma injection (*Huber et al. (2010), Huber et al.*
87 *(2011)*). However, thermomechanical remobilization is important only over long time
88 scales of 10^2 - 10^3 years, while on short time scales of 10^0 - 10^1 years magma injection
89 is the principal triggering mechanism of rhyolitic eruptions (*Huber et al. (2011), Hu-*
90 *ber et al. (2012); Degruyter and Huber (2014); Townsend et al. (2019)*). Other views
91 indicate that unrest on time scales of 10^0 - 10^1 years at large silicic systems may also
92 be explained by melt amalgamation resulting from the inherent instability of buoyant
93 melt layers (*Sparks et al., 2019*). Other views that consider non-magmatic processes
94 suggest that caldera unrest results from a combination of magma injection, volatile
95 exsolution and/or crystallization and degassing of large magma batches without new
96 inputs of magma. Caldera uplift is then punctuated by episodic leaks of fluids from
97 below the brittle-ductile transition (BDT) to shallow areas that deform in a brittle
98 way (*Fournier, 2007*). Further, seismic and geodetic data show that episodes of uplift
99 resulting from likely magma injections are transient features and can be separated by
100 many years (*Delgado et al., 2018; Druitt et al., 2019*) or even decades (*Sigmundsson*
101 *et al., 2010; Druitt et al., 2019*) without any other clear evidence for unrest. Other
102 views suggest that caldera resurgence is the direct consequence of episodic magma
103 injection resulting from the incremental and protracted growth of plumbing systems.
104 The episodic uplift is interrupted by episodes of deflation but the net result is uplift
105 (*Acocella, 2019*). Regardless of the mechanism of unrest, a key question in volcano
106 science still remains and has direct implications for models of hazard: when do these
107 pulses of uplift imply a potential eruption? (e.g., *Pritchard et al. (2019)*).

108 If these uplift events are in turn produced by magma injection, how many of them
109 and of what magnitude are required to actually trigger an eruption? Unfortunately,
110 some models used to study active intrusions (*Lengline et al., 2008*) do not have predic-
111 tive capabilities and cannot predict the maximum stress in the reservoir walls produced
112 by magma injection. This is a necessary element in eruption forecasting models be-
113 cause the rupture threshold for dike propagation towards the surface depends upon
114 the reservoir pressure. Dikes form when the deviatoric hoop stress in the reservoir
115 walls reaches a threshold above the tensile strength of the rock which is known to
116 be within ~ 1 - 40 MPa (*Tait et al., 1989; Albino et al., 2010*). Nonetheless, given our
117 imperfect knowledge of the shallow reservoir location, size and physicochemical state,
118 the exact rupture threshold is unknown. Furthermore, the maximum pressurization

119 that reservoirs sustain before an eruption likely varies throughout the lifetime of a single
 120 edifice and between different volcanoes (*Lu et al., 2003; Pinel et al., 2010; Carrier*
 121 *et al., 2015*).

122 In this study we focus on the episode of unrest during 2004-2009 at Yellow-
 123 stone (*Chang et al. (2007), Chang et al. (2010)*), the fastest ever recorded at that
 124 volcano since systematic geodetic measurements started in 1975 (*Pelton and Smith,*
 125 *1979*). Despite more than 4 decades of geodetic observations, there is still significant
 126 uncertainty on the driving mechanisms of ground deformation (*Dzurisin et al., 2012;*
 127 *Hurwitz and Lowenstern, 2014*). For example, a detailed conceptual model does not
 128 assess the relative contributions of basalt injections and exsolved volatiles (*Dzurisin*
 129 *et al., 2012*). We test the hypothesis of whether the 2004-2009 episode of unrest was
 130 caused by magma injection or other mechanisms, and particularly the nature of the
 131 fluids involved in the episodes of unrest (*Hurwitz et al., 2007a; Dzurisin et al., 2012*).
 132 To assess these questions, we use all the continuous GPS and all the ENVISAT InSAR
 133 data that recorded the complete 2004-2009 episode of uplift with improved source mod-
 134 els of ground deformation and solid-fluid mechanics models of magma injection. These
 135 models are a function of the magma viscosity, magma compressibility and conduit radi-
 136 us among other parameters, and can predict the time series of ground deformation
 137 (e.g., *Lengline et al. (2008); Le Mével et al. (2016); Delgado et al. (2018)*). We com-
 138 pare the deformation data and models with other seismic swarms in December 2008
 139 (*Farrell et al., 2010*) and January 2010 (*Shelly et al., 2013*) and discuss mechanisms
 140 of transition from caldera uplift to subsidence. We finally extend our models to the
 141 most recent periods of unrest during 2014-2015 (*Wicks et al., 2020*).

142 **2 Geological and ground deformation background of Yellowstone caldera**

143 Yellowstone caldera is a $\sim 85 \times 45$ km³ topographic depression and is the youngest
 144 of three collapse calderas in the Yellowstone plateau. The eruptions that formed these
 145 calderas occurred 2.1, 1.3 and 0.64 Myrs ago erupting the Huckleberry Ridge, Mesa
 146 Falls and Lava Creek Tuffs with erupted volumes larger than 2450, 280 and 1000
 147 km³ respectively (*Christiansen, 2001*). The last of these eruptions formed the current
 148 Yellowstone caldera, which is now filled with 600-1000 km³ of post caldera rhyolitic
 149 lava flows. Post caldera volcanism has been focused on the Sour Creek and Mallard
 150 Lake domes (SCD and MLD hereafter) (*Figure 1*) which have been active for the past
 151 0.164 Myrs (*Christiansen, 2001*). The caldera is underlain by a large plumbing system
 152 with large but spatially variable contents of melt (*Farrell et al., 2014; Huang et al.,*
 153 *2015; Schmandt et al., 2019*). Yellowstone hosts the largest hydrothermal system in the
 154 world with half of the world's geysers (*Hurwitz and Manga, 2017*) and several hundreds
 155 of hydrothermal vents (*Fournier, 1989; Lowenstern and Hurwitz, 2008; Hurwitz and*
 156 *Lowenstern, 2014*). On a geological time scale, the VEI 8 eruptions and the large
 157 hydrothermal activity are fuelled by large batches of basalt injection under the upper
 158 to mid-crustal silicic system, evidenced by a very large CO₂ degassing flux. This
 159 requires that the injecting basaltic magma has a CO₂ concentration of 400-500 ppm.
 160 Such a large amount of CO₂ cannot be dissolved in silicic melts because it would
 161 be completely exhausted in 1000 years. Mass balances indicate that ~ 0.3 km³/yr of
 162 basaltic melts are intruded beneath the caldera, a similar amount to that intruded at
 163 the Hawaii hot spot (*Lowenstern and Hurwitz, 2008; Lowenstern et al., 2015*). These
 164 injections are also the ultimate source of caldera unrest (*Wicks et al., 2006; Dzurisin*
 165 *et al., 2012*).

166 **2.1 Observations and models of caldera unrest**

167 A summary of geodetic observations of ground deformation between 1923 and
 168 2008 is described in detail in *Dzurisin et al. (2012)*. Ground deformation was observed

169 for the first time in 1975 when leveling lines were measured after 1923 recording 0.7 m
 170 of uplift, with a time-averaged rate of ~ 1.4 cm/yr (*Pelton and Smith, 1979*). Systematic
 171 time-lapse leveling started in 1983 until 2007, and showed that the caldera floor
 172 uplifted until 1984 when the uplift shifted to subsidence following the largest historical
 173 swarm ever measured at Yellowstone with M_C magnitudes up to 4.9 (*Waite and
 174 Smith, 2002*). Caldera subsidence continued until 1996 when a 1 year long episode of
 175 caldera uplift was recorded (*Wicks et al., 1998*). Coevally, the area of Norris Geyser
 176 Basin (NGB hereafter) uplifted between 1996 and 2000 (*Wicks et al., 2006*). Continuous
 177 GPS monitoring started in 1996 with a five-fold increase in the station density in
 178 2000 (*Figure 1*). In July 2004, the whole caldera floor uplifted in the largest episode
 179 of historic unrest with a maximum uplift rate of 7 cm/yr and with subsidence at rates
 180 of 2 cm/yr at NGB (*Chang et al. (2007), Chang et al. (2010)*). The caldera uplift
 181 ended in late 2009, coevally with another seismic swarm in the NW part of the caldera
 182 (*Shelly et al., 2013*). More recent episodes of unrest include uplift at NGB between
 183 December 2013 and March 30 2014, subsidence at NGB and uplift at the caldera between
 184 March 2014 and early 2015, and NGB uplift and caldera subsidence up until
 185 the present (*Dzurisin et al., 2019; Wicks et al., 2020*) (*Figure 1*). The transition from
 186 uplift to subsidence usually occurs with large seismic swarms at the distal parts of the
 187 caldera (*Waite and Smith, 2002; Shelly et al., 2013*).

188 Previous InSAR studies have focused on ERS-1/2 data to measure caldera floor
 189 subsidence during 1992 to 1995, slight caldera floor uplift during 1995-1996, uplift at
 190 NGB during 1996-2000 (*Wicks et al., 1998, 2006; Dzurisin et al., 1999; Dzurisin and
 191 Lu, 2007; Vasco et al., 2007; Aly and Cochran, 2011; Dzurisin et al., 2012; Tizzani
 192 et al., 2015; Dzurisin et al., 2019; Wicks et al., 2020*), caldera uplift with ENVISAT
 193 during 2004-2009 (*Chang et al. (2007), Chang et al. (2010), Aly and Cochran (2011),
 194 Dzurisin et al. (2012), Tizzani et al. (2015)*), and NGB uplift, subsidence and then up-
 195 lift with TerraSAR-X and Sentinel-1 data during December 2013 - March 2014, March
 196 2014 - early 2015 and then 2016 - 2017 respectively (*Dzurisin et al., 2019; Wicks et al.,
 197 2020*). Despite the good quality of the InSAR observations, all the previous studies
 198 have used a few interferograms only that provide individual snapshots of the individ-
 199 ual episodes of unrest. The only exception is *Tizzani et al. (2015)* who calculated an
 200 InSAR time series with a descending ERS/ENVISAT track for 1992-2010.

201 3 Data analysis and deformation results

202 3.1 InSAR and GPS data analysis

203 We use GPS data from the stations WLWY, LKWY, OFW2, HVWY and NRWY
 204 operated by the University of Utah and the EarthScope Plate Boundary Observatory,
 205 and processed by the *Nevada Geodetic Laboratory*. (*Figure 1, Figure S1*). These
 206 stations record the record the complete sequence of uplift and subsidence during 2004-
 207 2009 (*Figure 1*). We use InSAR data from the C-band ERS-1/2, ENVISAT, L-band
 208 ALOS and X-band TerraSAR-X satellites (*Table 1*) processed as both individual in-
 209 terferograms and InSAR time series depending upon the satellite platform, and data
 210 temporal resolution (*Figure 2 - Figure 3, Figures S2-S5*). Data processing follows
 211 standard procedures for time series analysis (e.g., *Doi et al. (2011)*) and is described
 212 in detail in the supplementary material. We calculate InSAR time series for the EN-
 213 VISAT data, and from this product we extract the cumulative ground deformation
 214 during the episode of uplift as the difference in deformation between the last image
 215 in 2009 and the first image in either 2004 or 2005 (*Table 1*). These data span the
 216 complete episode of caldera uplift and are hereafter referred as interferograms. For the
 217 TSX data we stack the data and instead calculate rate maps of mean ground velocity
 218 (supplementary material).

219

3.2 2004 - 2009 deformation

220

221

222

223

224

225

226

227

228

229

230

231

232

233

234

235

236

237

238

239

240

241

242

243

244

245

Despite the different amount of SAR images and the variable interferogram quality in the different ENVISAT tracks, each of the time series record a total of ~ 25 and ~ 20 cm of line-of-sight (LOS) uplift at SCD and MLD between September 2004 and September 2009 (Figure 2 - Figure 3). The InSAR data also record ~ 8 cm of subsidence at the NGB between 2004 and 2008 – one year before the end of the uplift at the resurgent domes (Figure 3). The wavelength of the deformation signals at SCD, MLD and NGB is constant during 2004-2009 and does not change during the recorded time span, indicating that the sources causing deformation do not change in depth (not shown). The GPS stations OFW2 located near the MLD, and the stations HVWY, LKWY and WLWY located near the SCD record between ~ 10 and 20 cm of uplift during the same time span, in agreement with them being at variable distances from the areas of maximum uplift (Figure 1). The deformation signals are similar in location and wavelength to those analyzed in previous studies (Chang *et al.* (2007), Chang *et al.* (2010); Aly and Cochran (2011); Tizzani *et al.* (2015); Wicks *et al.* (2020)). A seismic swarm that occurred in December 2008 and was detected by the LKWY station (Farrell *et al.*, 2010) is not observed by the InSAR data because we do not include winter images and because the geodetic signals it produced are below the InSAR uncertainty. No clear evidence of localized fault creep triggered by magmatic deformation was observed on any of the InSAR time series. The onset of deformation cannot be assessed from the InSAR data because there are only two non-winter images in 2004 (Figure S2). Both the GPS data for stations OFW2, HVWY, LKWY and WLWY and InSAR time series during 2004-2009 display a pattern of uplift in which deformation increases exponentially until a threshold is reached and followed by an exponential decrease (Figure 1, Figure 2, described later). This exponential increase followed by exponential decrease is referred to hereafter as double exponential (Le Mével *et al.*, 2015).

246

3.3 2010 - 2013 deformation

247

248

249

250

251

252

253

254

255

256

257

258

The caldera uplift transitioned to subsidence in January 2010 until December 2013. The GPS data recorded this with a constant rate of ~ 1.5 cm/yr, but only the ENVISAT IM2 descending data recorded it (Figure 2C), with an average subsidence of 1-2 cm. ALOS-1 interferograms display double-bounce signals in wetlands that introduce abrupt phase discontinuities (e.g., Wdowinski and Hong (2015)) and phase unwrapping errors that cannot be corrected. This data shows no deformation during 2010-2011, so it is not considered further in this study (Figure S5). The maximum caldera subsidence is at MLD instead of SCD, with a maximum of -3.5 to -2 cm/yr depending on the track and on the amount of data used in the stacks. The caldera deformation pattern of the January 2010 - December 2013 subsidence is significantly different to that of the 2004-2009 uplift (Figure 2F, G). The TSX and GPS data record no deformation at NGB during this time span.

259

4 Kinematic source modeling

260

261

262

263

264

265

266

267

268

To understand the sources responsible for the ground deformation at Yellowstone, we jointly invert the 2004-2009 interferograms and the GPS vectors with two sources. These include a tensile dislocation (Okada, 1985) representing an opening sill below the caldera floor plus an additional source to model the deflation below the NGB – either a pressurized small sphere (McTigue, 1987) or another tensile dislocation. We note that the combination of two Okada sills neglects the mechanical interaction between them (Pascal *et al.*, 2014), but from a computational point of view it is much faster to implement than a numerical model calculated with either finite or boundary element methods. We do not invert the 2010-2013 deformation data because the

269 TSX and the GPS data show velocity differences up to $\sim 50\%$. The wavelength of
 270 the deformation signals are on the order of several tens of kilometers, suggesting
 271 that the deformation sources are likely to lie below the BDT. However, [Tizzani et al.](#)
 272 (2015) has shown that viscoelastic effects representative of viscous rheologies are only
 273 relevant for time scales longer than 580 years which are well below the time span
 274 of ~ 5 years considered in this study. The interferograms were downsampled with
 275 a resolution-based algorithm ([Lohman and Simons, 2005](#)). Data were inverted with
 276 the neighborhood algorithm [Sambridge \(1999\)](#) (hereafter NA), a non-linear inversion
 277 method which iteratively searches for the best-fit model parameters avoiding local
 278 minima, and the Levenberg-Marquardt (LM) algorithm to search for global best-fit
 279 model. The inversion procedure is described in detail in the supplementary material.

280 4.1 Uniform opening model

281 The model of a horizontal sill below the caldera floor and a depressurized sphere
 282 below NGB do not produce a fit as nearly as good compared to that of two dislocations.
 283 Therefore we focus on a model of two Okada sills only. The best-fit geometry is made
 284 up of two horizontal sills ([Figure 4, Table 2](#)) at depths of 8.7 km for the caldera sill and
 285 10.6 km for the NGB sill ([Figure S6](#)). The vertical components of the WLWY, LKWY
 286 and OFW2 stations are almost insensitive to the closing of the NGB sill ([Figure S7](#)),
 287 therefore the time series of vertical displacement of these stations are proportional to
 288 the caldera sill opening. The sill centroid depths uncertainties are in [Figure S8](#).

289 The Okada model does not include the pressure change as a model parameter so
 290 we follow two approaches to estimate it. First, the area of the caldera source sill (\sim
 291 $58 \times 19 \text{ km}^2$) can be roughly approximated by that of three penny-shaped cracks with
 292 a radii $a = 9.7 \text{ km}$ for each one. Then, we use the formula $\Delta V = \frac{8}{3} a^3 (1 - \nu) \frac{\Delta P}{G}$ ([Fialko](#)
 293 [et al., 2001b](#)) to get an order of magnitude of the sill pressure change. This approach
 294 is just a very coarse approximation and does not imply that an Okada volume change
 295 is directly comparable to that of a pressurized penny-shaped crack. Using a volume
 296 change of $\Delta V \sim \frac{0.354}{3} \text{ km}^3$ for each of these sources, a Poisson ratio $\nu = 0.25$ and a
 297 shear modulus of $G = 2.1 \text{ GPa}$ ([Heap et al., 2020](#)) we get a source overpressure of 0.13
 298 MPa. Second, we use the boundary element software DEFVOLC ([Cayol and Cornet,](#)
 299 [1997](#)) to calculate the source overpressure (supplementary information). This model
 300 predicts sill depths of 14 and 17.5 km for the caldera and NGB sources respectively,
 301 and a pressure change of $\sim 0.08 \text{ MPa}$, which is 60% of the value inferred from the
 302 crack approximation ([Figure S9](#)). These sources are much deeper than those inferred
 303 from the inversion of the Okada models. The overpressure for both models are several
 304 orders of magnitude below the tensile strength of the encasing rocks of 10-40 MPa
 305 (e.g., [Albino et al. \(2010\)](#)).

306 4.2 Distributed sill opening model

307 The inversion for dislocations with uniform opening results in non-negligible
 308 residuals near MLD and SCD ([Figure S6](#)), which potentially result from localized
 309 areas of fluid pressurization below the resurgent domes. To improve the data fit, we
 310 use a distributed sill-opening model for the caldera sill at a depth of 8.7 km (e.g.,
 311 [Delgado et al. \(2018\)](#); [Henderson et al. \(2017\)](#)). In this model, the best-fit sill is aug-
 312 mented to 12×8 smaller sills, each one with an area of $5 \times 5 \text{ km}^2$, and we enforce the
 313 constraint that the sill opening tapers to zero at its edges ([Figure 4, Figure S10](#)). The
 314 distributed opening model predicts volume changes for the caldera source of 0.354 km^3
 315 during 2004-2009, 0.306 km^3 during 2005-2009, and a volume decrease for the NGB
 316 source of -0.121 km^3 and -0.0981 km^3 for the same time periods respectively. The
 317 time-averaged caldera sill opening is $0.07 \text{ km}^3/\text{yr}$. The distributed opening models
 318 show no clear boundary between the zones of volume change beneath SCD and MLD
 319 ([Figure 5](#)). A residual of $\sim 5 \text{ cm}$ is observed in the E part of Yellowstone Lake par-

320 ticularly in the ascending interferograms and could be related to the December 2008
321 seismic swarm ([Farrell et al., 2010](#)).

322 4.3 Temporal evolution of the sill opening model

323 The vertical components of the five GPS stations were inverted for the caldera
324 sill opening and NGB sill closing models for every epoch to retrieve the cumulative
325 volume change of the uniform opening model ([Figure 6](#)).

326 5 Dynamic source modeling

327 Kinematic source models like the aforementioned two sills do not provide in-
328 sights on the physical mechanism driving the caldera uplift. In this study we focus
329 solely on the mechanism of magma injection from a deep source to a shallow source
330 because there are simple analytic formulas that can be compared directly with ground
331 deformation time series ([Lengline et al., 2008](#); [Le Mével et al., 2016](#)). Although the
332 reviews of [Dzurisin et al. \(2012\)](#) and [Lowenstern et al. \(2015\)](#) suggest the role of both
333 hydrothermal and magmatic fluids, including exsolved volatiles from cooling magma,
334 in this study we neglect these effects. Hereafter we refer to magma as molten rock
335 with a Newtonian viscosity. This is a clear oversimplification of the very complex
336 hydrothermal-magmatic system of Yellowstone, but it is necessary to assess to what
337 extent ground deformation can be explained by one of these end-member models. In
338 the following we consider two cases. First, an analytic model of magma injection
339 below Yellowstone caldera. Second, a new analytic model of magma injection below
340 Yellowstone caldera from both a mantle source and from the reservoir below NGB.

341 5.1 A pressurized reservoir connected to a mantle magma source

342 We start with a magma injection model in which the caldera reservoir is connected
343 to a magma source in the mantle, whose source pressure function increases linearly
344 until a threshold t^* when it reaches a constant. Magma ascends due to its overpressure
345 and pressurizes the shallow reservoir, resulting in a double exponential function for
346 both the reservoir overpressure and the ground displacement ([Le Mével et al., 2016](#)).
347 This model does not take into account the potential connection between NGB and the
348 caldera source, which is addressed later in the study.

349 5.1.1 Mathematical background

350 The magma injection model is defined by [Equation 1- Equation 2](#).

$$351 P(t) = \begin{cases} \frac{st}{t^*} + (s\tau_p - \Delta\rho gL)(e^{\frac{-t}{\tau_p}} - 1) & 0 < t < t^* \\ st\left(\frac{\tau_p}{t^*}e^{\frac{-t}{\tau_p}} - \frac{\tau_p}{t^*}e^{\frac{-(t-t^*)}{\tau_p}} + 1\right) & t > t^* \end{cases} \quad (1)$$

$$352 \tau_p = \frac{8\eta LV(\beta_w + \beta_m)}{\pi R^4} \quad (2)$$

353 Here, $P(t)$ is the pressure in the deep mantle source, t^* is the transition time
354 between linear increasing and constant deep pressurization, τ_p is a constant that de-
355 pends on the properties of the plumbing system, R is the conduit radius, L is the
356 conduit length, V is the reservoir volume, β_w and β_m are the reservoir and magma
357 compressibility, s is the pressurization rate, $\Delta\rho$ is the density difference between the
358 magma and host rock, and g is the gravity acceleration. Since the source pressure is
proportional to the displacement for pressurized cavities embedded in a linear-elastic
half-space ([McTigue, 1987](#)), the model can be scaled with an arbitrary constant to

359 model the GPS time series (e.g., [Henderson et al. \(2017\)](#)). In this case, $P(t)$ is an
 360 adimensional pressure function because there is no analytic expression to convert the
 361 pressure to displacement with the Okada model. Further, if no changes occur in the
 362 plumbing system, like a change in the source geometry, then transient changes in the
 363 time series are direct evidence of transient changes in the reservoir pressure and
 364 ultimately in the deep source pressure function. As stated earlier, the InSAR data
 365 does not show changes in the wavelength of the deformation signals so the sources
 366 are fixed in depth. This way, we know that changes in the time series do not result
 367 from changes in the source geometry. Nevertheless, the magma composition cannot be
 368 estimated without inferences on the conduit radius (e.g., [Pedersen and Sigmundsson](#)
 369 [\(2006\)](#); [Fukushima et al. \(2010\)](#); [Delgado et al. \(2018\)](#)) and the source volume ([Segall,](#)
 370 [2019](#)), the latter of which is not available from the Okada model.

371 **5.1.2 Inverse models**

372 Inversions for the best-fit magma injection model using the InSAR and the ver-
 373 tical component of the WLKY GPS time series for the SCD predict similar time con-
 374 stants ([Figure 7a](#)), but a shorter transition for the InSAR-derived model parameters.
 375 This is due to the lack of InSAR data between September 2004 and May 2005 and the
 376 higher uncertainty of InSAR with respect to GPS. Therefore, the InSAR data are not
 377 considered further for these dynamic models. If the GPS stations record deformation
 378 produced by a single source, then the source pressure function is the same for all of
 379 them. The only difference between the time series is the deformation amplitude which
 380 is a function of the source geometry and is a constant for each GPS station. Hence the
 381 time series can be normalized to account for this constant ([Figure 7b](#)). The best-fit
 382 magma injection model with no buoyancy ($\Delta\rho = 0$) for the normalized vertical com-
 383 ponent of the WLWY, LKWY and OFW2 stations predicts a transition time of 0.66
 384 years and an exponential time constant of 4 years, with a final adimensional amplitude
 385 of 1.37. The magma injection model predicts significant ground uplift for at least 5
 386 additional years should inelastic effects be absent. The magma injection model is also
 387 applied to GPS time series during 2014-2015, when fast uplift at NGB transitioned to
 388 subsidence following a Mw 4.9 earthquake on March 30 2014. The model results in
 389 good data fits ([Figure 8](#)), but the prediction of a double exponential is nearly identical
 390 to that of the single exponential model. In this latter model the pressure in the deep
 391 magma source is constant during the whole episode ([Lengline et al., 2008](#)). The InSAR
 392 and GPS data and the magma injection model suggest that caldera uplift at Yellow-
 393 stone during 2004-2009 and 2014-2015 is directly indicative of magma injection into
 394 the caldera source with no need for pressurization due to volatile exsolution at the top
 395 of the plumbing system or at the bottom of the shallow hydrothermal system. This
 396 is in contradiction with a hybrid model of magma injection and volatile exsolution
 397 ([Dzurisin et al., 2012](#)). The magma injection model also ignores the contemporary
 398 deflation at NGB, which we address in the following section.

399 **5.2 Two pressurized reservoirs connected to a mantle magma source**

400 The geodetic data show that uplift at the caldera floor is coeval to subsidence at
 401 the NGB during most of the 2004-2009 episode of unrest, and that two sub-horizontal
 402 sills are responsible for the deformation signals. In this section we use a simple fluid-
 403 solid mechanics model based on mass conservation to unravel the potential connection
 404 between these two sources of deformation. We test the hypothesis that uplift at the
 405 caldera can be explained by magma injection from both the mantle and the NGB
 406 sources ([Figure 9](#)). As our goal is to provide a simple physical model that allows
 407 us to understand, not model the GPS time series, we make several geometrical and
 408 mechanical simplifications.

409 The model of magma flow for two deformation sources embedded in a homoge-
 410 neous linear elastic half-space is based on a mass balance that couples the reservoirs
 411 volume and pressure changes with the Poiseuille flow law. These equations are pre-
 412 sented in previous studies (*Lengline et al., 2008; Segall, 2013; Reverso et al., 2014; Le*
 413 *Mével et al., 2016; Walwer et al., 2019*) and we adapt them for the specific case of
 414 Yellowstone. We do consider the effect of magma compressibility due to variations in
 415 the reservoir pressure (*Rivalta, 2010*). More complex rheologies like elastic layering,
 416 viscoelasticity or other mechanisms of fluid transfer such as flow in a poroelastic me-
 417 dia (*Hurwitz et al., 2007a*) are not considered in this study. Also, the model considers
 418 neither the mechanical interaction between the sources (*Pascal et al., 2014*) nor the
 419 lateral offset between the sill centroids which are not symmetric and do not lie on top
 420 of each other. We assume that since the sources are very large, these boundary effects
 421 have a secondary effect. For simplicity we also neglect the short time lag between the
 422 onset of inflation at SC and ML and the deflation at NGB. We also neglect the com-
 423 plexity of Yellowstone’s plumbing system inferred from seismic tomography (*Farrell*
 424 *et al., 2014; Huang et al., 2015*), including large areas of partial melt and multiphase
 425 components in the magma (crystals, dissolved and exsolved CO₂ and H₂O). We also
 426 neglect the lateral magma transfer and storage between SCD and MLD (*Figure 5*),
 427 because these effects are of secondary order with respect to a single zone of magma
 428 accumulation along the two domes (*Figure 4, Figure S6*). Since the pressure is pro-
 429 portional to the displacement in a linear elastic half-space, ground deformation follows
 430 the same trend as the source pressure function.

431 5.2.1 Mathematical background

432 The volume change rate in the two reservoirs connected with each other, were one
 433 of them is fed by a mantle magma source (*Figure 9*), is derived from mass conservation
 434 and is given by *Equation 3 - Equation 4* (e.g., *Reverso et al. (2014); Walwer et al.*
 435 *(2019)*)

$$\frac{d\Delta M_s}{dt} = \rho_m \frac{d\Delta V_s}{dt} = \rho_m(Q_{in} + Q) \quad (3)$$

$$\frac{d\Delta M_d}{dt} = \rho_m \frac{d\Delta V_d}{dt} = -\rho_m Q_{in} \quad (4)$$

436 with $\Delta M_s, \Delta M_d$ the mass change in the shallow (*s*) and deep reservoirs (*d*), ρ_m
 437 the magma density, $\Delta V_s, \Delta V_d$ the volume change in the shallow and deep reservoirs, Q
 438 the volume flux from a deep mantle source, and Q_{in} the volume flux from the NGB to
 439 the caldera source reservoir. Here the shallow and deep reservoirs represent the caldera
 440 source and the NGB sill-like sources. The relation between the volume change $\Delta V_{s,d}$
 441 and the resulting reservoir overpressure $\Delta P_{s,d}$ under the assumption that magma is
 442 incompressible and the density is constant is *Equation 5*

$$\Delta V_{s,d} = \Delta P_{s,d} \frac{\pi a_{s,d}^3 \gamma}{G} \quad (5)$$

443 with γ equal to 1 for a sphere (*McTigue, 1987*) and $\frac{8(1-\nu)}{3\pi}$ for a penny-shaped
 444 crack (*Fialko et al., 2001b*), G the shear modulus and $a_{s,d}^3$ the sphere/crack radius.

445 The volume flux in a vertical conduit connecting a mantle magma source $\Delta \bar{P}$ to
 446 a shallow source ΔP_s is given by the Poiseuille law in *Equation 6*

$$Q = \frac{\pi a^4}{8\mu H} (\Delta \rho g H + \Delta \bar{P} - \Delta P_s) \quad (6)$$

447 with a the conduit radius, μ the magma viscosity, H the conduit length, $\Delta\rho$
 448 the magma-host rock density contrast, g the gravitational acceleration and $\Delta\bar{P}$ the
 449 mantle magma pressure (*Jaupart and Tait, 1990; Lengline et al., 2008*). The expres-
 450 sion is nearly identical for the conduit connecting the shallow and the deep source in
 451 [Equation 7](#)

$$Q_{in} = \frac{\pi a_2^4}{8\mu_2 H_2} (\Delta\rho_2 g H_2 + \Delta P_d - \Delta P_s) \quad (7)$$

452 with H_2 , a_2 and μ_2 the conduit length, radius and magma viscosity and ΔP_d
 453 the deeper reservoir pressure. Here the flow from the deep reservoir depends upon
 454 the pressure gradient (*Segall, 2013*) instead of a constant magma flow (*Reverso et al.,*
 455 [2014](#)). Combining [Equation 3](#) - [Equation 7](#) results in two equations for the pressure
 456 change of the two pressurized reservoirs ([Equation 8](#) - [Equation 9](#)).

$$\frac{d\Delta P_s}{dt} = \frac{a_2^4 G}{8\mu_2 H_2 a_s^3 \gamma} (\Delta\rho_2 g H_2 + \Delta P_d - \Delta P_s) + \frac{a^4 G}{8\mu H a_s^3 \gamma} (\Delta\rho g H + \Delta\bar{P} - \Delta P_s) \quad (8)$$

$$\frac{d\Delta P_d}{dt} = -\frac{a_2^4 G}{8\mu_2 H_2 a_d^3 \gamma} (\Delta\rho_2 g H_2 + \Delta P_d - \Delta P_s) \quad (9)$$

457 We set

$$\begin{aligned} \tau_2^{-1} = \beta &= \frac{a_2^4 G}{8\mu_2 H_2 a_s^3 \gamma} \\ \tau_1^{-1} = \alpha &= \frac{a^4 G}{8\mu H a_s^3 \gamma} \\ \tau_3^{-1} = \epsilon &= \frac{a_2^4 G}{8\mu_2 H_2 a_d^3 \gamma} \end{aligned} \quad (10)$$

458 Instead of a piecewise mantle source pressure function of a linear increase followed
 459 by a constant after a time threshold (*Le Mével et al., 2016*), we use an exponential
 460 function of the form $\Delta\bar{P} = \bar{P}(1 - e^{-\frac{t}{\tau_m}})$ because it is easier to integrate. We use $\tau_m =$
 461 0.36 years from the data ([Figure 7](#)).

462 The solution method is outlined in the supplementary material. The final solution
 463 for initial conditions $P_s(0) = 0, P_d(0) = P_{d_0}$ is [Equation 11](#)

$$\begin{bmatrix} \Delta P_s \\ \Delta P_d \end{bmatrix} = C_1 e^{\lambda_1 t} \begin{bmatrix} 1 + \frac{\lambda_1}{\epsilon} \\ 1 \end{bmatrix} + C_2 e^{\lambda_2 t} \begin{bmatrix} 1 + \frac{\lambda_2}{\epsilon} \\ 1 \end{bmatrix} + \begin{bmatrix} a_1 \\ a_2 \end{bmatrix} e^{-\frac{t}{\tau_m}} + \begin{bmatrix} b_1 \\ b_2 \end{bmatrix} \quad (11)$$

464 with the eigenvalues $\lambda_{1,2}$

$$\lambda_{1,2} = \frac{-(\alpha + \beta + \epsilon) \pm \sqrt{(\alpha^2 + \beta^2 + \epsilon^2 + 2\alpha\beta + 2\beta\epsilon - 2\alpha\epsilon)}}{2} \quad (12)$$

465 and constants

$$\begin{aligned} b_1 &= \bar{P} + \Delta\rho g H \\ b_2 &= \bar{P} + \Delta\rho g H - \Delta\rho_2 g H_2 \\ C_1 &= P_{d_0} - (C_2 + a_2 + b_2) \\ C_2 &= \epsilon \frac{(P_{d_0} - a_2 - b_2)(1 + \lambda_1/\epsilon) + a_1 + b_1}{\lambda_1 - \lambda_2} \end{aligned} \quad (13)$$

Here P_{d_0} is the overpressure produced by injection of basaltic magma at the NGB reservoir during 1996-2000 (Wicks *et al.*, 2006). Since basaltic magma is unlikely to significantly cool to produce a significant density and viscosity change in 4 years, for simplicity we assume that $\Delta\rho = \Delta\rho_2$, $\mu = \mu_2$.

The selected model parameters are in Table 3. Since there are no geophysical constraints on the fourth power of the conduit radius R^4 and the viscosity of the injecting basalt μ , we parametrize the model in terms of the conduit conductivity $\bar{c} = R^4/\mu$ (Anderson and Segall, 2013). Basaltic melts have viscosities of $10 - 10^2$ Pa s (Giordano and Dingwell, 2003) and conduit flow models during episodes of unrest in basaltic volcanoes show radii of ~ 1 m (Pedersen and Sigmundsson (2006); Fukushima *et al.* (2010)), resulting in $\bar{c} \sim 0.1 - 0.01 \frac{m^4}{Pa \cdot s}$. The initial pressure with respect to lithostatic conditions are $P_s^0 = 0$ MPa and $P_d^0 = 0 - 0.5$ MPa, the latter value arising from the potential magma injection at NGB during 1996-2000 (Wicks *et al.*, 2006). The amplitude of the source pressure just scales the pressurization of the reservoirs, so it is not relevant since we are interested in the temporal evolution of the reservoir pressures. We consider cases with and without a magma density difference, in which the magma ascends due to its overpressure and due to the combined overpressure and buoyancy effects.

5.2.2 Forward models

The simulations show that magma ascent due to its overpressure predicts double exponential pressure functions for both the caldera and the NGB sources, albeit with a lower amplitude for the latter (Figure 10a-b). For $P_d^0 = 0$ MPa, the model cannot predict a linear depressurization for the NGB source. The model implies that magma ascends from the mantle to the shallow reservoir, and then the high magma overpressure drives magma 2 km down into the NGB reservoir, which is unrealistic. Magma compressibilities for a gas-poor basalt have a second order effect and do not change the predicted pressure change (not shown), but increasing the magma compressibility significantly increases the amount of intruded magma (e.g., Figure 9 in Le Mével *et al.* (2016)). When magma ascends due to its buoyancy and overpressure, the model predicts double exponential pressurization at the caldera source and both depressurization and pressurization at NGB with near linear trends (Figure 10c-d). We note that the magnitude of the pressurization of the buoyancy and overpressure model is one order of magnitude larger than the model with magma overpressure only.

The only possibility to significantly depressurize the NGB source due to magma flow to the caldera source is to set $P_d^0 = 0 - 0.5$ MPa (Figure 11b,f) and with $\bar{c} \sim 10^0 \frac{m^4}{Pa \cdot s}$ or smaller. As this value is increased, the magnitude of the subsidence decreases in response to a better hydraulic connection. The simulation predicts depressurization at NGB and double exponential pressurization at the caldera, but eventually all the subsidence from material extracted from NGB is counterbalanced by the fluid influx from the caldera source to NGB. The MBEM model predicts $\Delta P \sim 0.08$ MPa for the caldera source, so it is very unlikely that the NGB reservoir overpressure reached 0.5 MPa during the 1996-2000 episode of unrest because uplift during that time span was much lower than the caldera uplift during 2004-2009 (Figure S4, Figure 2). This implies that the NGB reservoir should have been pressurized decades before 1996, which is a geologically plausible scenario (Wicks *et al.*, 2020), but for which we have no quantitative constraints.

An alternative model considers that the mantle magma source is located below NGB instead below the caldera. Here magma ascends to NGB, and then from NGB to the caldera sill (Reverso *et al.*, 2014), potentially resulting in depressurization during several years at NGB. In this case the second term in the right hand side of Equation 8 must be moved in the right hand side of Equation 9, after switching ΔP_s with ΔP_d

and modifying the time constant of this term with factors appropriate for the NGB reservoir. We also assume a slight overpressure for the NGB source. In this model the NGB source deflates for ~ 1.5 years, while the caldera source inflates with an exponential. Afterwards, both sources linearly inflate (not shown), which does not match the trends recorded in the GPS data.

Regardless of the model, none of these simulations can predict at the same time the trends observed in the InSAR and GPS time series at both the caldera floor and NGB and with a constrained set of assumptions available since geodetic measurements only started in 1975.

6 Discussion

6.1 Source models and comparison with previous studies

Two families of source models have been proposed for the 2004-2009 episode of unrest: those that rely on horizontal dislocations (*Chang et al. (2007)*, *Chang et al. (2010)*; *Wicks et al. (2020)*, this study) and those that use a combination of pressure sources (*Aly and Cochran, 2011*; *Tizzani et al., 2015*). Although both types of models can fit the data well, we consider that the dislocations are more realistic. First, they require less model parameters. Second, neglecting the mechanical interaction between two sills is less inaccurate than neglecting the interaction between at least three pressure sources (*Aly and Cochran, 2011*; *Tizzani et al., 2015*). Our results are similar to those of *Chang et al. (2007)* and *Chang et al. (2010)* who also found two rectangular dislocations at depths of ~ 7 -10 and ~ 7 -13 km for the caldera and NGB sources, albeit modeling very small data sets. The caldera source model is located at the top of the low V_P zone below the caldera imaged with three-dimensional P wave tomography. This zone has -3 to -4% of V_P difference with respect to the reference velocity model and is inferred to contain little to no partial melt resolvable by this geophysical method (*Farrell et al., 2014*; *Huang et al., 2015*). Since magma injection is a discrete event with respect to the spatially and time averaged resolution of seismic tomography, we see no contradiction between the geodetic sources and lack of a clear V_P anomaly. *Wicks et al. (1998, 2006)* have argued that two discrete sources of deformation exist below the caldera floor, and are episodically active over different times. However, both the uniform and distributed (*Figure 4*, *Figure S6*) opening models indicate that a single dislocation can explain most of the deformation signal during 2004-2009. The caldera source has no clear boundary between the magma accumulation zones below SCD and MLD, except for localized uplift at the SCD, resulting in an additional 5 cm of uplift with respect to MLD. Given the few cycles of deformation observed with detailed geodetic observations, it is not possible to assess if the discrete storage zones below the MLD and SCD (*Wicks et al., 2006, 1998*) are representative of caldera uplift during longer periods of time. The NGB source is significantly shallower with respect to the source that uplifted during 1996-2000 located at a depth of 14 km (*Wicks et al., 2020*), vs 10.7 during 2004-2009. However, *Wicks et al. (2020)* concluded that the same NGB source can model the 1996-2000, 2004-2009 but with different amounts of sill opening and closing. Another difference with respect to *Chang et al. (2007)* and *Chang et al. (2010)* models is that a significant part of the NGB source is located below the caldera floor, and not adjacent to it.

Changes in the source geometry can be assessed comparing the location and wavelength of the deformation signals for the different episodes of uplift for InSAR data that were acquired with the same or very similar flight direction, radar beam and look angle. These data sets include ERS-1/2 descending interferograms and a stack (*Figure S4*), the ENVISAT IM2 data (*Figure 2*) and the TSX descending stack. Here the ERS-1/2 and ENVISAT IM2 data have the same line-of-sight. This analysis shows that the wavelength and location of the deformation signals varies during the periods of caldera

568 subsidence in 1992-1995 (*Wicks et al. (1998)*; *Aly and Cochran (2011)*, Figure S4),
 569 uplift in 1996-1997 (Figure 2F in *Wicks et al. (1998)*), subsidence in 2000-2002 (Figures
 570 2b-c in *Wicks et al. (2006)*), uplift in 2004-2009 (Figure 2), subsidence in 2010-2013
 571 (Figure 2), uplift in 2014-2015 (*Wicks et al. (2020)*, Figure 8) and subsidence in 2015-
 572 2020 (Figure 1 in *Wicks et al. (2020)*). The deformation signals at NGB also shows
 573 differences in location and wavelength during the episodes of unrest between in 1996-
 574 2008 (*Wicks et al. (2020)*, Figure 2, Figure S4), uplift during early 2014, subsidence
 575 during the rest of 2014 and uplift during 2015-2019 (Fig 2b-c in *Wicks et al. (2020)*).
 576 This implies that the deformation sources are not stable during several cycles of uplift
 577 and subsidence, and they slightly change from one cycle to the next one. In contrast,
 578 other volcanoes show stable deformation sources over several cycles of deformation,
 579 even after eruptions (*Lu et al., 2010*; *Lu and Dzurisin, 2010*; *Delgado, 2020*). The lack
 580 of stationary sources indicates patterns of migrating fluids towards shallower depths
 581 (*Wicks et al., 2020*) and hampers the use of magma dynamics models that rely on
 582 a single stable source in depth and location to explain long cycles of unrest (e.g.,
 583 *Giudicepietro et al. (2017)*). The spatial variability also indicates a highly dynamic
 584 plumbing system, akin to a crystal mush where unrest occurs episodically and in
 585 discrete zones of the mush (*Cashman et al., 2017*). On the other hand, we can ask:
 586 does the deformation data indicate a trans-crustal magmatic system in which unrest
 587 occurs at multiple depth levels in the crust? The variability in the source depths
 588 suggests that this actually occurs at Yellowstone, even on short time scales of less
 589 than one year, like during the NGB uplift in early 2014 (Figure 1). However, the exact
 590 pattern of fluid migration, potential magma mixing and mingling and stress interaction
 591 (e.g., *Albino and Sigmundsson (2014)*) are yet to be unravelled.

592 6.2 Driving mechanisms of unrest

593 On a geological time scale, the driving mechanism of unrest at Yellowstone
 594 caldera is discrete pulses of basalt injection at the base of the rhyolitic plumbing
 595 system below the caldera and NGB. *Lowenstern and Hurwitz (2008)* calculated that
 596 $\sim 0.3 \text{ km}^3/\text{yr}$ of basalt intrusion with 1 wt% of dissolved CO_2 is required to account
 597 for the measured flux of passive CO_2 degassing at Yellowstone, 4 times larger than
 598 the time-averaged rate of $\sim 0.07 \text{ km}^3/\text{yr}$ during 2004-2009. A direct comparison be-
 599 tween these data sets is not possible due to the episodic nature of magma injection
 600 and the lack of continuous time-lapse measurements of CO_2 degassing, discussed in
 601 detail later. The mechanisms of unrest are less clear over shorter time scales due to the
 602 coupling of the shallow hydrothermal system with the deeper magmatic system and
 603 volatile exsolution from the injecting basalt (*Dzurisin et al., 2012*). Also, independent
 604 data sets and models suggest contradicting mechanisms. Yellowstone lake shorelines
 605 have tilted terraces such that the caldera subsidence slightly exceeds caldera uplift
 606 during the Holocene (*Pierce et al., 2002*). To account for the slight subsidence, the
 607 volume change of exsolved volatiles extracted from the caldera must exceed the volume
 608 of injected magma, and these events must alternate in time. This leads *Pierce et al.*
 609 (*2002*) to suggest that the buildup and extraction of magmatic volatiles is a more likely
 610 explanation for the slightly higher subsidence in the Holocene than magma injection.
 611 Further, *Fournier (1989)* showed that a crystallizing magma can release $0.026 \text{ km}^3/\text{yr}$
 612 of exsolved fluids from the magma trapped below a self-sealed layer. This is enough
 613 to account for the volume changes that produced the caldera uplift during 1923-1975.
 614 The swarms are likely due to the episodic breaching of a self-sealed layer at the BDT
 615 that leads to fluid extraction from the caldera (*Waite and Smith, 2002*). This process
 616 is highly enhanced by a deepening of the BDT, produced by an increase in the strain
 617 rate due to episodic magma injection (*Fournier, 2007*), contradicting the previous
 618 mechanisms for unrest due to volatile pressurization and extraction.

619 Thereby, *Dzurisin et al. (2012)* favor a conceptual model that reconciles a wide
 620 range of geological, geochemical and geophysical observations. This model suggests

621 that episodic batches of basalt are injected at the base of the rhyolitic crystal mush
 622 resulting in reservoir pressurization either at NGB or SCD. As the basalt and the mush
 623 crystallize, magmatic volatiles are exsolved. These fluids are in a supercritical state
 624 that are trapped below a self-sealed layer in the lower parts of the hydrothermal system
 625 and the upper section of the magmatic system resulting in reservoir pressurization and
 626 caldera uplift. The self-sealed layer is also the BDT. Magma injection increases the
 627 strain rate, which temporarily deepens the BDT. In this scenario, fluids in the plastic
 628 zone at near lithostatic pressures eventually breach the self-sealed layer, leading to
 629 seismic swarms in distal parts of the caldera (*Waite and Smith, 2002*), fluid migration
 630 outside of the caldera and ground subsidence (*Fournier, 1989, 2007*). Long-term sub-
 631 sidence at the caldera is likely produced by volatile exsolution from the crystallizing
 632 rhyolitic mush that also migrates outside of the caldera (*Dzurisin et al., 1990*). How-
 633 ever, the *Dzurisin et al. (2012)* model does not allow for the assessment of the relative
 634 contributions of magma injection and volatile exsolution in the reservoir pressurization
 635 (e.g., *Tait et al. (1989)*) and the fluids sink sources. Therefore, we compare our results
 636 with the previous studies.

637 The LKWY, WLWY and OFW2 GPS fit to the magma injection model (*Fig-*
 638 *ure 7*) is a strong indication that the driving mechanism of uplift for the caldera source
 639 is the injection of $\sim 0.354 \text{ km}^3$ of incompressible basalt during 2004-2009, with no need
 640 to argue for exsolved volatiles (discussed later). In this model the pressure of the
 641 deep magma source increased linearly until it reached a threshold in early 2005, then
 642 it remained constant. This results in a time-variable uplift rate that increased expo-
 643 nentially and then decreased exponentially after 2005, until the hydraulic connection
 644 with the deep mantle source was shut down by inelastic processes (discussed later).
 645 Magma is injected in the upper part of the mushy plumbing system inferred from
 646 seismic tomography (*Farrell et al., 2014; Huang et al., 2015*). This is also valid for
 647 the caldera uplift during 2014-2015, in which magma was also likely injected, with a
 648 source pressure function that was different to that of the 2004-2009 episode, and with
 649 an unclear connection between the caldera and NGB sources. On the other hand,
 650 there are significant differences. First, the NGB reservoir during 2014-2015 is signifi-
 651 cantly shallower at a depth of 1-4.5 km (*Wicks et al., 2020; Dzurisin et al., 2019*) vs
 652 10.7 km for 2004-2009, leading *Wicks et al. (2020)* to suggest a source of hydrothermal
 653 origin. Therefore, we discard that the subsidence at NGB during 2014 would result
 654 from magma transfer from this source into the much deeper caldera source, located
 655 at a depth of ~ 6 km during 2014 (*Wicks et al., 2020*). Hence, the model of two con-
 656 nected reservoirs cannot be applied to this episode of uplift. We speculate that the
 657 reversal from uplift to subsidence at NGB in March 2014 resulted from fluid migra-
 658 tion into the shallow hydrothermal system following the breaching of the self-sealed
 659 layer that separates the BDT. Since the caldera source did not change its behaviour
 660 when NGB uplifted in early 2014 (*Figure 8*), we speculate that the BDT breaching
 661 might have changed the stress field in the deeper source (e.g., *Albino and Sigmunds-*
 662 *son (2014)*), potentially allowing for magma to be injected from a mantle source. The
 663 exact mechanism is beyond the scope of this study.

664 A significant caveat of the magma injection models is that they do not consider
 665 the complex structure of Yellowstone's underlying plumbing system inferred from local
 666 and teleseismic tomographies (*Farrell et al., 2014; Huang et al., 2015*). These studies
 667 show that the volcano is underlain by a low V_p anomaly at depths of 5-17 km with
 668 5-15% of melt fraction interpreted as a rhyolitic partial melt underlain by basaltic
 669 partial melt. Another low velocity zone is located at depths of 20 to 50 km, with a
 670 melt fraction of 2%, extending to the Moho and also interpreted as basaltic partial
 671 melt. The two low velocity zones are physically separated. The magma injection
 672 models considered in this study do not consider how magma bypasses or interacts in
 673 some way with these very large areas of partial melt, nor how the melt can segregate
 674 through the porous crystalline matrix to ascend through the crystal mush that likely

675 exists in the upper crust. Further, the magma injected during 2004-2009 likely has a
676 basaltic chemical composition compared to that of the mushy rhyolitic reservoir, and
677 they might eventually coalesce on time scales of 10^4 - 10^4 years (e.g., [Biggs and Annen](#)
678 [\(2019\)](#)). Magma can also stall somewhere in the crust in a level of neutral buoyancy
679 and undergo viscosity changes resulting in reservoir pressurization. Despite the data
680 show that the deformation sources do not change during the episode of uplift, it is
681 unclear how the ascending basalt interacts with the plumbing system in the framework
682 of a transcrustal model of unrest on multiple levels in the crust ([Cashman et al., 2017](#);
683 [Sparks et al., 2019](#); [Sparks and Cashman, 2017](#)). These are all points that have to be
684 addressed in future studies that relax the restrictive assumptions made in the models
685 of magma injection ([Figure 9](#)).

686 The spatial coincidence of the SCD with the area of maximum uplift has led
687 other studies to suggest that this is the main area of magma injection ([Wicks et al.,](#)
688 [2006](#); [Chang et al., 2007](#)). Despite the fact that uplift started simultaneously for SCD
689 and MLD in July 2004, we see no clear evidence in the OFW2, WLWY and LKWY
690 stations ([Figure 1](#), [Figure S1](#)) to state that magma was first intruded at SCD and then
691 it migrated to MLD, or that magma was injected at MLD and then was stored at SCD.
692 Whatever the situation, this suggests a highly connected area of magma storage that
693 responded coevally to the onset of magma injection with no clear boundary as shown
694 by the distributed sill opening models ([Figure 5](#)). GPS observations in the middle of
695 the caldera floor might help to address this point during future episodes of unrest.

696 Magma ascent resulting in reservoir pressurization is due to both its overpressure
697 and its buoyancy with respect to the host rock ([Equation 6-Equation 7](#)). The model of
698 connected reservoirs provides insights in this aspect ([Figure 10](#)). First, the model with
699 both magma buoyancy and magma overpressure is unable to reproduce the double
700 exponential signals observed at the caldera floor and the NGB, indicating that the
701 signal observed in the GPS time series is indicative of magma overpressure only. This
702 is not a unique characteristic of Yellowstone and has been observed at other volcanoes
703 (e.g., [Le Mével et al. \(2016\)](#)). Second, if buoyancy effects are neglected, then the
704 NGB source inflates in response to the magma flux, resulting in a pressure function
705 very similar to that of the caldera source, but this is not observed. Whatever the
706 case, the model suggests that magma ascends solely due to its overpressure, and that
707 the subsidence at NGB cannot be explained by a mechanism of magma flow with
708 Newtonian viscosity extraction towards the caldera source.

709 Any mechanism that explains the subsidence at NGB must take into account the
710 very similar onset of uplift with respect to the caldera source, and that the subsidence
711 at NGB ends as the caldera uplift decreases. This implies that the subsidence is
712 therefore triggered by magma injection at the caldera. The hydrothermal system is
713 shallower than 5 km ([Fournier, 1989](#)), so the 2004-2009 NGB source is too deep to
714 be considered of hydrothermal origin. [Chang et al. \(2007\)](#) explained the subsidence at
715 NGB with a mechanism in which the caldera sill opening produces positive dilatation
716 up to 3×10^{-5} strain next to the crack tip. This value is one order of magnitude above
717 the smallest measured strain change produced by dynamic earthquake triggering that
718 can induce transient increases in the medium permeability ([Manga et al., 2012](#)). This
719 mechanism can induce flow of magmatic volatiles from NGB to the caldera and trigger
720 microseismicity between these two sources. Although the mechanism is plausible, there
721 is a caveat. The NGB sill is located below the BDT and the surrounding medium
722 is plastic with little to no permeability that fluids can use to migrate between the
723 sources. Therefore an opening sill should not produce an increase in the medium
724 permeability because there is no primary porosity ([Fournier, 2007](#)). The permeability
725 can be increased by magma injection which increases the strain rate, deepening the
726 BDT by ~ 1 km, resulting in a change in the rheological properties and bringing deep
727 zones that are plastic into a brittle behavior for a short period of time. However, the

728 NGB and caldera sills lie at depths of 8.7 and 10.6 km (Figure S8), too deep to lie in
 729 the brittle region even after the transient increase in the strain rate. Further, lowering
 730 the BDT usually results in the breaching of the layer that separates the BDT, not in
 731 fractures in zones that are deep into the plastic zone. This implies that the permeability
 732 mechanism of magma transport is also not feasible and the connection between NGB
 733 and the caldera is uncertain.

734 We have shown that the geodetic signals during the episode of caldera uplift
 735 can be explained entirely by magma injection, with no need to invoke volatile ex-
 736 solution. But this model is neither unique nor necessarily the best explanation. It
 737 does not imply that during other episodes of ground uplift magma injection or other
 738 mechanisms of unrest can also produce the exact same geodetic signal. For example,
 739 rhyolitic plumbing systems are crystal mushes (e.g., *Bachmann and Bergantz (2008)*)
 740 and Yellowstone's plumbing system has limited amounts of melt (*Farrell et al., 2014*;
 741 *Huang et al., 2015*). Here, exsolved fluids can percolate through the porous matrix
 742 and ascend to the top of the mush where they accumulate in sill-like discrete areas.
 743 As the volume of fluids increases this can also result in sill pressurization and ground
 744 deformation (*Sparks et al., 2019*). Therefore, we can ask: is it possible that the fluid
 745 exsolution, permeable flow and fluid accumulation at the liquid-rich mush cap does
 746 not result in detectable pressurization during the caldera uplift? Is it possible that
 747 any significant fluid exsolution occurs only in response to the depressurization of the
 748 self-sealed layer after it is breached? This seems unlikely. For example, fluid exsolution
 749 is not enhanced if the minimum principal stress equals the lithostatic load until the
 750 latter equals the pore-fluid pressure (section 10.4.2 in *Fournier (2007)*), and this could
 751 be attained only after a certain amount of magma has been injected. Further, the
 752 mechanisms can vary significantly from an episode to the next one (*Fournier, 2007*),
 753 and mechanisms of unrest that last $10^0 - 10^1$ years might not be representative of the
 754 overall caldera behaviour during time scales of $10^4 - 10^5$ years (*Pierce et al., 2002*).
 755 These scenarios were not considered in this study but are geologically plausible, so
 756 future studies should address them.

757 **6.3 Comparison with seismicity, microgravity and stream/gas geochem-** 758 **istry**

759 Ground deformation is one of the several indicators of volcano unrest but uncer-
 760 tainties in the mechanisms that result in ground uplift imply that these data should
 761 be analyzed and compared jointly with other independent data sets (*Pritchard et al.,*
 762 *2019*). Here we compare the deformation during the episode of uplift with the dense
 763 seismic (*Waite and Smith, 2002*; *Farrell et al., 2014*) and geochemical (*Lowenstern*
 764 *et al., 2017*) data acquired during more than 30 years at Yellowstone.

765 Statistics of the number of earthquakes per quarter do not show any abnormal
 766 trends during 2004-2008 (Figure 1B in *Chang et al. (2007)*, *Chang et al. (2010)*, Fig-
 767 ure 8 in *Shelly et al. (2013)*, Figure 1 in *Farrell et al. (2014)*). The largest clusters
 768 of earthquakes with $M_L > 2.5$ in the caldera during the episode of uplift (Figure 1)
 769 occurred during 2004-2006 with microseismicity located at the northern edge of the
 770 caldera floor (*Chang et al. (2007)*, not shown in Figure 1), and during the December
 771 2008 swarm at Yellowstone Lake (*Farrell et al., 2010*). The seismicity at the onset of
 772 uplift is scattered across the caldera with no clear clusters and significantly less than
 773 the seismicity triggered when the uplift transitions to subsidence (*Shelly et al., 2013*).
 774 Focal mechanisms calculated from waveform first arrivals show normal faulting with
 775 seismicity clusters towards the N and S parts of the caldera and with only four events
 776 at the SCD (*Russo et al., 2017*). *Taira et al. (2010)* analyzed five M3+ earthquakes
 777 during 2007-2009, and two of these events were the first non-double couple focal mech-
 778 anisms since monitoring started in 1975. These earthquakes are triggered by fluid
 779 migration due to an increase in dilatation from the sill towards shallower opening

780 cracks. *Farrell et al. (2009)* calculated the b-value from the Gutenberg-Richter law in
781 a de-swarmed earthquake catalog from 1973 to 2006, showing high b-values next to
782 MLD, but no abnormal values indicative of fluid injection at the SCD. We conclude
783 that the 2004-2009 caldera uplift was not related to abnormal seismicity in response
784 to magma injection compared with the seismic swarms when deformation shifts from
785 uplift to subsidence (*Waite and Smith, 2002; Shelly et al., 2013*). This is in contrast
786 with other volcanoes, like Long Valley caldera where the onset ground uplift is corre-
787 lated with increases in seismicity (Fig 3a in *Hill et al. (2020)*). The lack of abnormal
788 seismicity during 2004 is not unique to Yellowstone, as other volcanoes with very fast
789 deformation, either basaltic like Sierra Negra (*Davidge et al., 2017*), or rhyolitic like
790 Cordón Caulle (*Delgado et al., 2018*) are accompanied by limited amounts of seismic-
791 ity. One potential explanation for the overall lack of abnormal seismicity is that the
792 plastic rocks around the rhyolitic reservoir cannot be fractured except at the end of
793 the cycles of uplift when the rocks behave in a brittle way for short periods of time.
794 Another alternative is that the 2004-2009 cycle of uplift did not produce significant
795 seismicity due to the Kaiser effect (*Heimisson et al., 2015*). Here fracturing and seis-
796 micity are produced only if the medium is stressed above a threshold in a loading cycle
797 that had already resulted in fracturing. However, this hypothesis can not be proved
798 as either true or false because only two cycles of uplift in 1923-1984 and 1996-1997
799 before 2004 were recorded with instrumental observations, both with a significantly
800 worse temporal sampling than the 2004-2009 cycle.

801 Micro-gravity data were only measured during 2007-2012 (*Farrell, 2014*), and
802 then since 2017 (*Poland and Zeeuwvan Dalfsen, 2019*). The 2007-2012 data did not
803 show clear gravity changes but as the data did not include high quality elevation
804 measurements for each gravity station, it did not provide insights on any particular
805 geological process (*Poland and Zeeuwvan Dalfsen, 2019*). Therefore the gravity data
806 cannot be directly compared with the InSAR and GPS observations during 2004-2009.
807 *Poland and Zeeuwvan Dalfsen (2019)* measured gravity variations four times during
808 2017 and concluded that the gravity uncertainty of ~ 20 mGal on stable benchmarks
809 is low enough to detect mass changes due to magma injection.

810 In terms of gas and fluid geochemistry, despite the many decades of sampling
811 at Yellowstone's hydrothermal fields (e.g., *Lowenstern et al. (2017)*), there is a dearth
812 of long-term geochemical time series. Continuous measurements of CO₂ with eddy
813 covariance instruments have been underway only since 2016 (*Lewicki et al., 2017*).
814 High temporal resolution water chemistry measurements at the Upper Geyser Basin
815 during 2007-2008 (*Hurwitz et al., 2012*) and in major rivers during 2001-2004 and
816 2006-2007 (*Hurwitz et al. (2007b), Hurwitz et al. (2010)*) cannot be compared with the
817 episode of caldera uplift due to their low temporal sampling, or being too distant from
818 the areas of unrest. Decadal time-lapse measurements are only available for chloride
819 discharges in streams with a yearly temporal sampling, but these measurements did not
820 show any unambiguous trend that deviates from the base level values during the period
821 of caldera uplift (*Hurwitz and Lowenstern, 2014*). Furthermore, a lateral redistribution
822 of the abnormal chloride flux due to basalt injection would take years to decades until
823 it would result in abnormal fluxes in streams and therefore correlations with ground
824 deformation are not expected to be detected (*Hurwitz et al., 2007b*). These authors
825 also concluded that it would be more feasible to detect perturbations in the shallow
826 hydrothermal system due to deep magma injection by tracking changes in the gas and
827 steam flux instead of the river solute fluxes. Finally, the correlation between older
828 episodes of unrest with geochemistry of springs in the NW part of the caldera do not
829 provide meaningful insights (*Evans et al., 2006*).

830 We conclude that the 2004-2009 episode of caldera uplift was not correlated
831 with other large-scale signs of unrest except during the December 2008 dike intrusion

832 (*Farrell et al., 2010*) and the transition from uplift to subsidence in January 2010
 833 (*Shelly et al., 2013*).

834 **6.4 Eruptive potential of Yellowstone**

835 Eruptions occur under tensile failure when the deviatoric stress in a pressurized
 836 reservoir reaches the tensile strength of the rock ($\sim 10\text{-}40$ MPa), and resulting in a mode
 837 I crack that propagates to the Earth surface (*Tait et al., 1989; Pinel and Jaupart,*
 838 *2003; Albino et al., 2010*). Other studies show that shear failure occurs before tensile
 839 failure (*Gerbault, 2012*). We use the source pressure change as a proxy for the tensile
 840 strength of the encasing rock at Yellowstone’s magma reservoir. The MBEM inversion
 841 predicts source overpressures of ~ 0.08 MPa (Figure S9), several orders of magnitude
 842 below the tensile strength of the rock (~ 10 MPa). Therefore individual pulses of
 843 uplift like those in 2004-2009 are very unlikely to lead to an eruption, unless the
 844 reservoir is very close to failure, for which there is no evidence. Eruptions should occur
 845 every ~ 100 cycles of uplift similar to that of 2004-2009. The recurrence interval of
 846 large-scale caldera uplift and then pressurization is not well constrained since geodetic
 847 observations with yearly temporal resolution started in 1975. If pressurization cycles
 848 last on the order of ~ 5 years, the eruption recurrence is at least 500 years, although
 849 there is considerable uncertainty because the caldera uplift is highly transient, with
 850 variable duration and length of the quiescence periods. If we assume that for every
 851 episode of uplift there is an episode of quiescence or caldera subsidence of similar
 852 duration, then the eruptive frequency increases to 1,000 years. The last eruptions
 853 at Yellowstone occurred ~ 70 Kyr ago (*Christiansen, 2001*), which is more than one
 854 order of magnitude longer than our eruption interval. If the net record of deformation
 855 in the Holocene is slight subsidence, it implies that reservoir deflation is slightly larger
 856 than reservoir pressurization and hence the pulses of uplift are even less likely to result
 857 in an eruption (*Pierce et al., 2002*).

858 Despite the small amount of pressurization, which are much lower than pressure
 859 changes in smaller sills elsewhere (e.g., *Le Mével et al. (2016); Delgado et al. (2016)*),
 860 a seismic swarm interpreted as a small dike intrusion occurred in December 2008 -
 861 January 2009. The material that intruded the dike was either rhyolitic magma or
 862 magma-derived aqueous fluids (*Farrell et al., 2010*). The dike is offset with respect
 863 to the locus of maximum magma injection at the SCD. This dike produced small
 864 displacements recorded by the LKWY station (< 1 cm, *Farrell et al. (2010)*), but the
 865 distributed opening model shows residuals in the eastern part of Yellowstone Lake that
 866 could be explained by this small dike (Figure 4). One explanation is that this intrusion
 867 was triggered by reaching the tensile strength of the rock after thousands of loading
 868 cycles. Another alternative is that successive cycles of uplift and subsidence at the
 869 caldera floor might have decreased and permanently fractured the surrounding rock
 870 due to damage loading, effectively lowering the wall rock shear modulus and decreasing
 871 the rupture threshold (*Carrier et al., 2015*). If this is true, cyclic pressurization that is
 872 unable to trigger a dike intrusion under the aforementioned standard rupture models
 873 (*Pinel and Jaupart, 2003; Tait et al., 1989; Albino et al., 2010*) can result in small dike
 874 intrusions that would not be observed otherwise. Another alternative is that these
 875 rupture criteria are not valid for the geologic conditions of Yellowstone due to the
 876 very large plumbing system of this volcano and the weak surrounding crust. Another
 877 alternative is that it was not a dike intrusion but only a small swarm (*Shaul Hurwitz,*
 878 *personal communication*). A final alternative is that the swarm was produced by
 879 leakage of a small amount of magmatic fluids above the BDT, but with no resulting
 880 subsidence until the next leakage one year later. Whatever the case, the eruptive
 881 potential of Yellowstone deserves a more thorough analysis relating the cyclic loading
 882 model with a detailed analysis of the seismic data (e.g., *Carrier et al. (2015)*).

883

6.5 Transition of uplift to subsidence

884

885

886

887

888

889

890

891

892

893

894

895

896

897

898

899

900

901

902

903

904

One of the most intriguing features of Yellowstone is the cyclic transition of uplift to subsidence with periods of ~ 10 years (Figure 1). This transition has been explained by the breaching of a self-sealed layer at the BDT due to transient pressurization by either magma injection or exsolved fluids which migrate outside the bounds of the caldera upon the layer breaching (Waite and Smith, 2002; Dzurisin et al., 2012). The fluid migration occurs at the end of an uplift cycle and is coeval with seismic swarms in the distal parts of the caldera (Waite and Smith, 2002; Shelly et al., 2013). Afterwards, the caldera subsides in response to migration of exsolved fluids from a crystallising mush for several years until another cycle resumes (Dzurisin et al., 1990). Volumetric changes due to a cooling intrusion produce negligible volume changes and are unable to explain the caldera subsidence (Dzurisin et al., 1990). In this model of cyclic deformation, the secular trend of subsidence due to volatile exsolution is reversed by highly transient pulses of basalt injection at the caldera, as in 2004-2009. The Madison Plateau swarm in January 2010 (Shelly et al. (2013), Figure 1) is interpreted as the breaching of the self-sealed layer in the NW part of the caldera, and occurred during the transition from uplift to subsidence. In general, non-eruptive subsidence at volcanoes and calderas like Cerro Blanco (Pritchard and Simons, 2004), Askja (de Zeeuw-van Dalfsen et al., 2013) and Medicine Lake (Poland et al., 2006) show linear rates of ~ 2 -3 cm/yr on time spans of decades. These have been related to cooling intrusions and a combination of other mechanisms like tectonic extension, but in the absence of a clear sink area, the exact mechanism of subsidence is quite uncertain.

905

906

907

908

909

910

911

912

913

914

915

916

917

918

919

920

921

922

923

924

925

926

927

928

929

930

931

The InSAR and GPS observations raise more questions than answers on the mechanisms of caldera subsidence. First, what is the sink of the magmatic fluids extracted from the NGB? Wicks et al. (2020) suggested that fluids extracted from NGB are injected either in the Norris-Mammoth corridor or the Hebgen Lake fault zone which are the zones with the highest amount of seismicity at Yellowstone. None of the post 2010 data show clear deformation signals outside of the caldera that could be sink sources for some fluids extracted from NGB and the caldera, although the small swath of the TSX data also introduces some uncertainty in this regard (Figure 2). It is also possible that the escaping fluids do not leave a clear geodetic signal if there is no sink reservoir to store them. This is in contrast with the post 2014 deformation which shows small-scale deformation that could reflect fluid pathways outside of the caldera (Fig 7 in Wicks et al. (2020)). Second, if the end of the caldera uplift is due to some inelastic mechanism of fluid migration above the BDT, then it implies that breaching the self-sealed layer changed the force balance on the conduit that feeds the caldera reservoir. Fluid migration outside of the caldera source implies that the pressure gradient driving this flow is much higher than the pressure gradient between the caldera and the mantle source, suggesting a feedback mechanism. We speculate that the breaching of the self-sealed layer stopped the connection between the deep mantle and the caldera sources as the magma injection model predicts several years of continuing uplift had the breaching not occurred (Figure 7). From a fluid mechanics point of view, this situation is analogous to reservoirs that were inflating prior to an eruption and erupt with reservoir deflation and without co-eruptive magma recharge (e.g., equation 7 in Segall (2013), equation S.29 in Delgado et al. (2019)). Finally, the pattern of cyclic uplift and subsidence (Figure 1) indicates that Yellowstone might behave as a harmonic oscillator with periods of ~ 10 years (e.g., Walwer et al. (2019)), and this should also include the effect of viscoelastic relaxation on time scales of several decades. More geodetic data recording future episodes of unrest will shed light on this.

932

7 Conclusions

933

934

In this study we revisit InSAR and GPS time series that span the 2004-2009 episode of ground uplift at Yellowstone caldera, the largest instrumentally detected

935 at this volcano. For the first time, simple solid and fluid mechanics models derived
936 from geophysical data provide quantitative evidence that the caldera uplift during this
937 time period results from magma injection from a deep mantle source into a shallow
938 source at ~ 8.7 km. Magma ascent and injection results only from its overpressure, not
939 from the effects of buoyancy. In contrast, transient increases in permeability and/or
940 magma extraction from the NGB source towards the caldera source cannot explain the
941 subsidence that is recorded at the former area. The caldera uplift can be modeled with
942 no need to invoke pressurization due to exsolved volatiles, which raises the question on
943 the non-uniqueness of models that can explain the geodetic observations. In general,
944 the episode of uplift was only related to small increases in the microseismicity in areas
945 neighboring the caldera, with no clear correlation with other instrumental observations.
946 A more complete view of episodes of unrest can result from a more integrated view of
947 the different geochemical, geodetic and seismological data sets. Future studies should
948 consider more complex mechanisms of volatile exsolution, stress-driven fluid migration
949 and abrupt changes in the force balance that drives the fluid transport and storage
950 between the caldera, the NGB source and potential sink regions.

951 **Acknowledgments**

952 F.D. acknowledges the French Centre National d'Etudes Spatiales (CNES) for a post-
953 doctoral fellowship, Charles Wicks (U.S. Geological Survey) for discussions and grant-
954 ing access to TSX data, Valérie Cayol (Université Clermont Auvergne) for her help
955 with the [DEFVOLC](#) boundary element software, Tara Shreve (Carnegie Institution for
956 Science), Michael Poland, Jacob Lowenstern, Shaul Hurwitz (U.S. Geological Survey),
957 Juliet Biggs (University of Bristol) for discussions, and Paula Burgi (Cornell Univer-
958 sity) for her grammar review. The InSAR data was processed at IGP's S-CAPAD
959 cluster and we thank Geneviève Moguilny for her help with this computing facility.
960 We thank Editor Paul Tregoning and two anonymous reviewers for their comments
961 that improved the quality of the manuscript. This is IGP contribution XXXX.

962 **Data Availability statement**

963 ERS-1/2 and ENVISAT data are property of the European Space Agency (ESA)
964 and were provided through [GEO Geohazard Supersites and Natural Laboratories](#) and
965 [UNAVCO](#). ALOS-1 data are property of the Japanese Ministerium of Trade and Com-
966 merce and were provided by NASA through the [Alaska Satellite Facility](#). TerraSAR-X
967 data are property of Deutsche Zentrum fr Luft- und Raumfahrt (DLR) and are avail-
968 able at [UNAVCO](#) upon request to Principal Investigator Charles Wicks (USGS). GPS
969 data were provided by [Nevada Geodetic Laboratory](#) and also available by the [USGS](#)
970 [Earthquake Hazard Program](#). Earthquakes in [Figure 1](#) are from the [USGS Earthquake](#)
971 [Catalog](#).

Tables

Satellite	λ (cm)	Dates (yyyy/mm/dd)	Pass	Path	θ	Mode, Beam	#SAR	#Ifg	Atmcor	DEMcor
ENVISAT	5.56	2004/09/03 - 2010/09/17	A	48	19	IM1	26	14	no	no
ENVISAT	5.56	2004/09/22 - 2009/10/21	A	320	23	IM2	26	42	ERAW2	yes
ENVISAT	5.56	2005/05/24 - 2010/08/31	D	313	19	IM1	12	10	ERAW2	no
ENVISAT	5.56	2005/05/05 - 2010/10/21	D	41	23	IM2	28	37	ERAW2	yes
ALOS-1	23.8	2006/12/30 - 2011/02/25	A	197	38	FBD-FBS	15	7	linear	no
ALOS-1	23.8	2007/01/16 - 2011/03/14	A	198	39	FBD-FBS	19	N/A	N/A	N/A
TerraSAR-X	3.1	2011/07/23 - 2013/07/07	A	45	21	strip_003	12	2*	no	no
TerraSAR-X	3.1	2011/07/28 - 2013/10/19	A	121	35	strip_009	16	3*	no	no
TerraSAR-X	3.1	2011/07/19 - 2013/10/10	D	159	28	strip_006	10	6*	no	no

Table 1: Details of the processed SAR data sets. The columns show the satellite name, radar wavelength (λ), date range (year/month/day), whether the satellite is in an ascending (A) or descending (D) orbit, satellite path, average incidence angle (θ), radar beam except for ALOS-1 where it indicates the radar mode (either FBD or FBS, Fine Beam Double and Fine Beam Single polarization), number of synthetic aperture radar images (SAR) per track, and the number of interferograms used in the time series (Ifg). The asterisk indicates the number of stacked interferograms instead of the number pairs used in the time series inversion. Atmcor is the type of atmospheric correction applied to the data: ERAW2 atmospheric correction with the ERA5 model and an empirical correction with an elevation-dependent term on top of that. DEMcor refers to whether a DEM error correction (*Ducret et al., 2014*) was used or not.

Source model	X_s (km)	Y_s (km)	Z_s (km)	L (km)	W (km)	θ	δ
Sill caldera floor	537.0**	4933.2**	8.7 **	57.6**	18.6**	54*	0*
Sill NGB	528.1**	4940.0**	10.6 **	22.6	26.6	357	0*

Table 2: Best-fit sill models. X_s centroid EW coordinate, Y_s centroid NS coordinate, Z_s centroid depth, a major semi axis, b semi-minor axis. Centroid coordinates are in WGS84 UTM 12N datum. Model parameters were iteratively inverted for. First we fixed parameters with * since they converge much faster than any of the others in the NA inversion. After many iterations we fixed the parameters with **. Finally we inverted the rest of the NGB model parameters .

G (GPa)	ν	H (km)	H_2 (km)	a_s (km)	a_d (km)	γ	$\Delta\rho$ (kg/m ³)	V_{R_s} (km ³)	V_{R_d} (km ³)	β_m (Pa ⁻¹)
2.1	0.25	10	2	15	10	$\frac{8(1-\nu)}{3\pi}$	270	1000	100	0.1×10^{-10}

Table 3: Parameters for the analytic model of magma injection connecting two reservoirs. G from *Heap et al. (2020)*, H_2 and H from the best-fit sill inversion (*Table 2*), γ for the crack-like sill reservoirs.

Figures

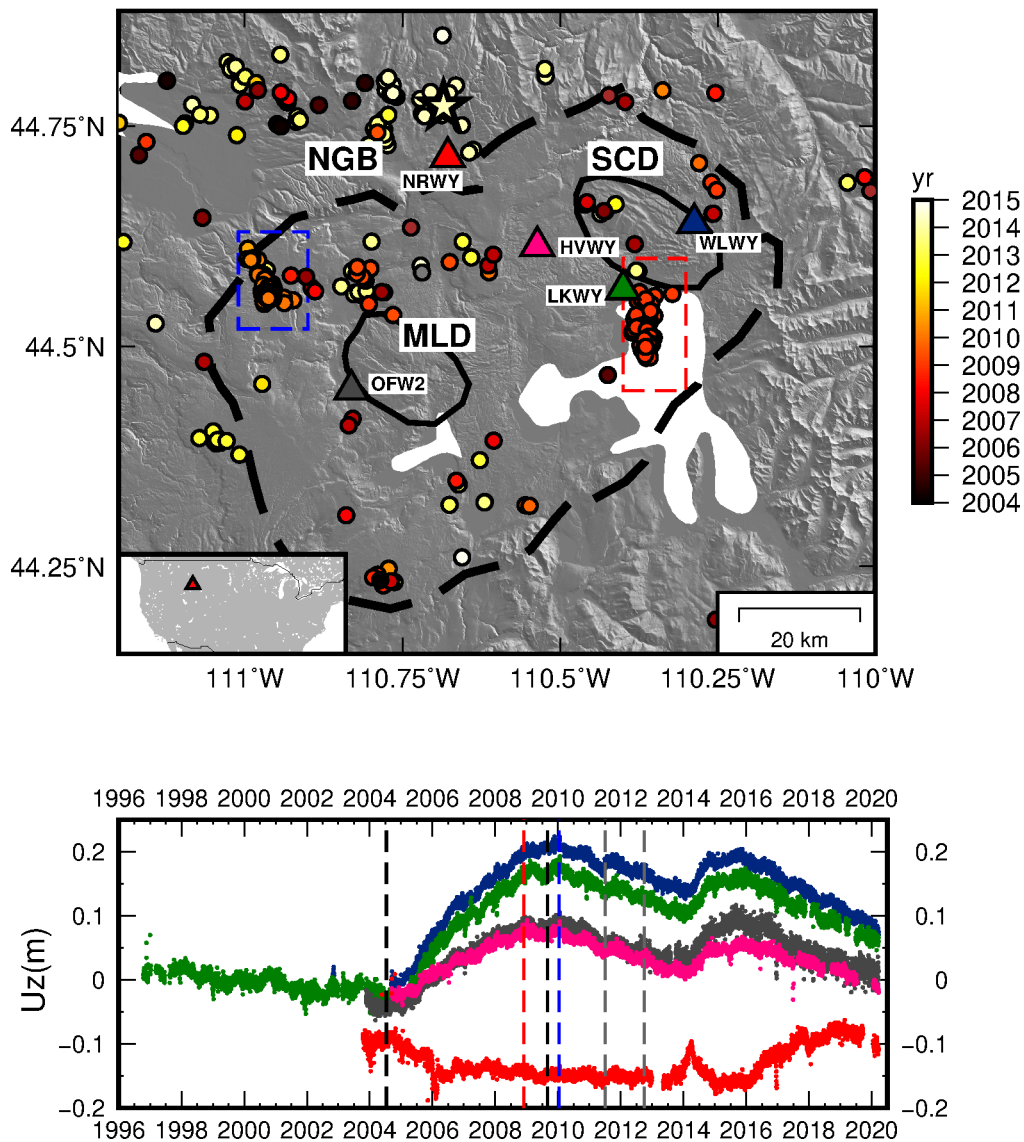


Figure 1: Top. Yellowstone caldera (thick dashed line), Mallard Lake (MLD) and Sour Creek (SCD) resurgent domes (black lines) draped over the 10m shaded NED DEM. Triangles are GPS stations that recorded data during the complete episode of unrest in 2004-2009. The dots show earthquakes from the [USGS Earthquake Catalog](#) shallower than 15 km with $M_L > 2.5$. The red and blue dashed rectangles show the December 2008 ([Farrell et al., 2010](#)) and January 2010 Madison Plateau ([Shelly et al., 2013](#)) seismic swarms. The star is the M_W 4.8 earthquake of March 30 2014 at NGB. Inset shows location of Yellowstone caldera (red triangle) within the United States. Bottom. GPS time series of vertical deformation (colored triangles on top). The dashed black and grey lines show the 2004-2009 episode of unrest, and the caldera subsidence covered by the TSX data during 2011-2012 respectively. The vertical red and blue lines show the December 2008 and January 2010 seismic swarms.

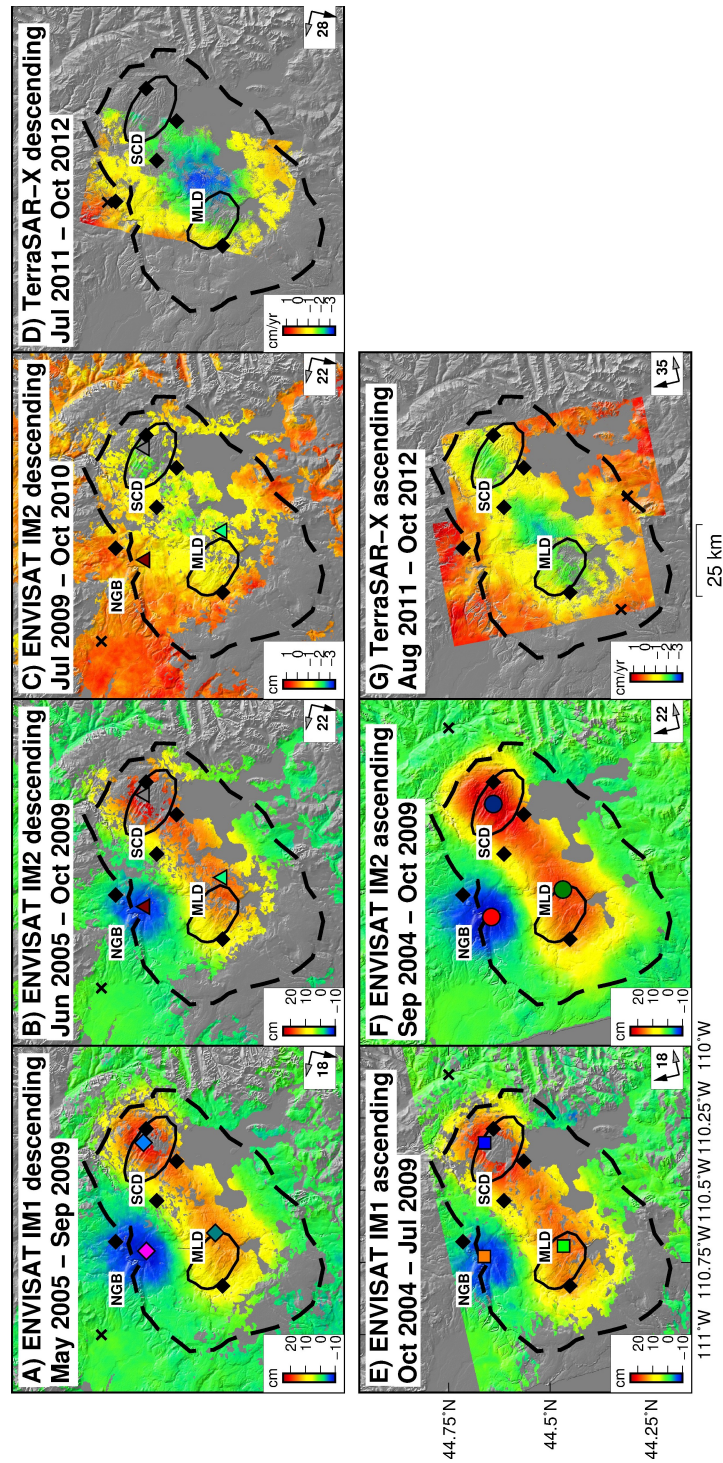


Figure 2: ENVISAT interferograms that record the total displacement at Yellowstone during 2004-2009 from InSAR time series (A, B, C, E, F, units in cm), and mean ground velocities from TSX stacks (D, G, units in cm/yr). The dashed black line is the caldera border and the thin black lines show the MLD) and (SCD). NGB is the Norris Geyser basin. The black diamonds are the continuous GPS stations used in the study (Figure 1). The black crosses are the reference point for each time series. The colored circles, squares, triangles and diamonds in (A, B, C, E, F) show the location of maximum uplift for MLD and SCD, and subsidence for NGB in the time series in Figure 2.

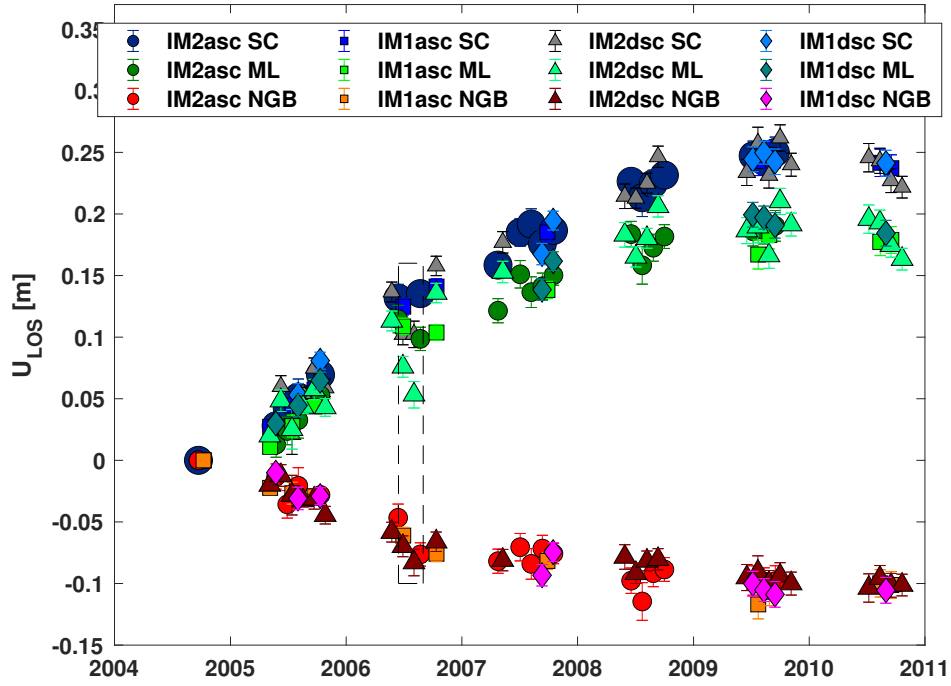


Figure 3: ENVISAT time series for selected pixels of maximum displacement at SCD, MLD and NGB (Figure 2). The IM2dsc data show larger dispersion in the displacement because the interferograms used in the time series contain far more turbulent signals than any of the other three tracks (Supplementary Material). The dashed box shows jumps in the IM2 descending time series not observed in other data sets. Using pairwise logic, these are not indicative of any ground deformation signal.

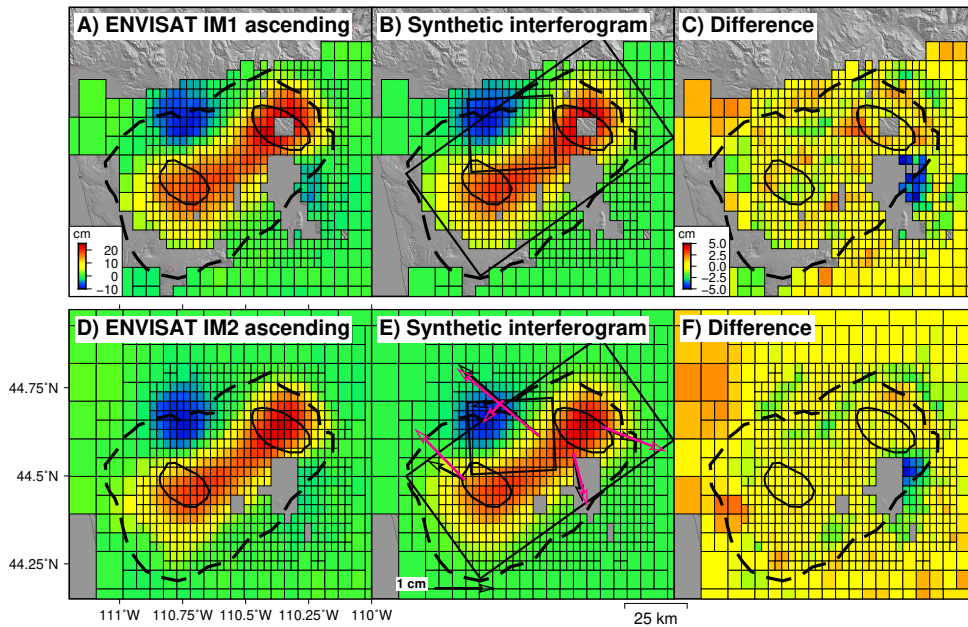


Figure 4: Downsampled (A, D), synthetic (B, E) and residual interferograms (C,F) produced by an opening sill below the caldera and by a closing sill below NG spanning 2004-2009. The black and pink arrows are the GPS data and synthetic data from the best-fit joint inversion. The rectangles are the modeled sills (Figure 5).

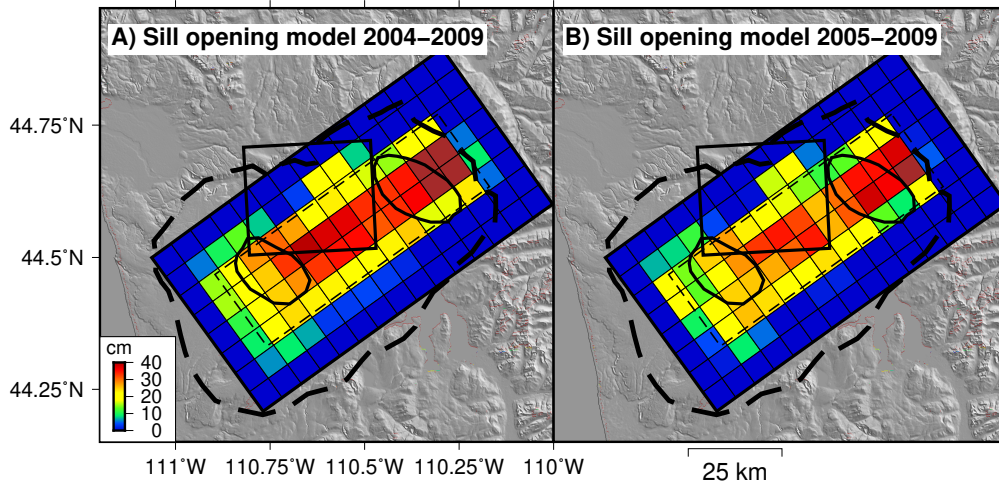


Figure 5: Distributed sill opening models for 2004-2009 (A) and 2005-2009 (B). The thin and dashed rectangles are the NGB and the caldera sources with uniform opening. The thick dashed line is the caldera border and the elliptical polygons are the SCD and MLD.

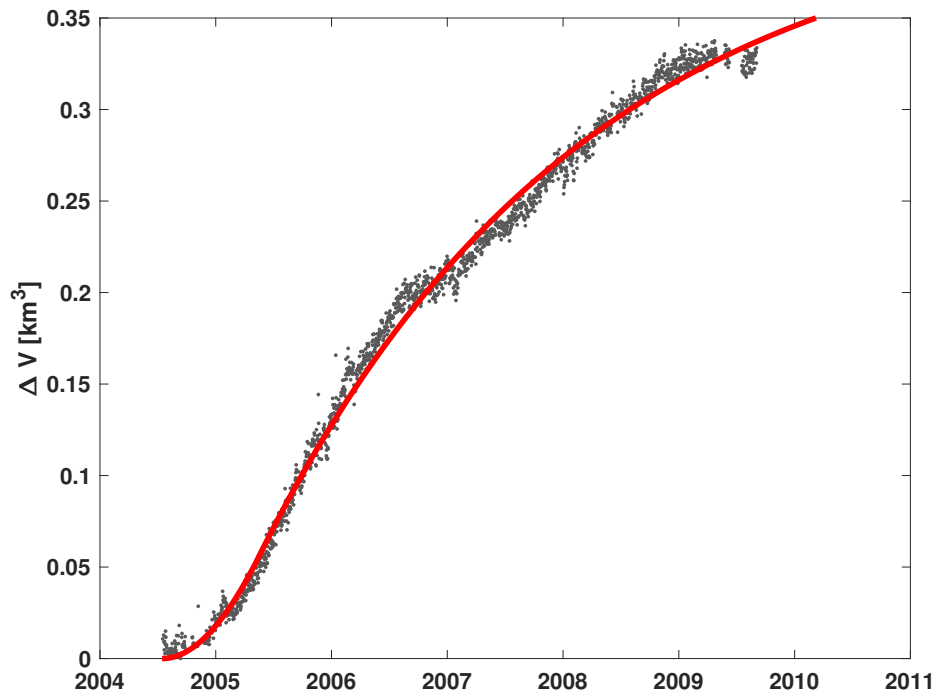


Figure 6: Time series of volume change (ΔV) for the caldera floor source with uniform opening, and inverted from the vertical component (U_z) of all the GPS stations. The red line is the best-fit Equation 1, but with P scaled to represent the source volume change.

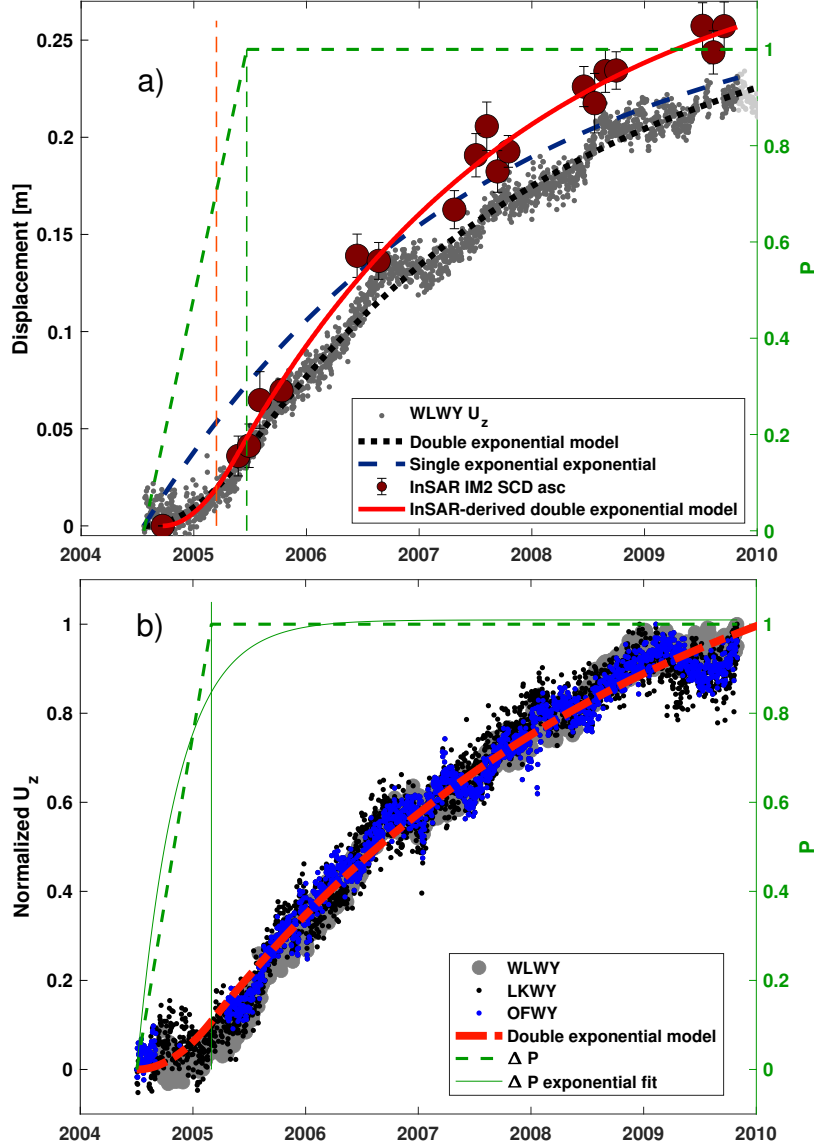


Figure 7: A. Magma injection model fits to GPS (grey dots) and InSAR (red circles) data. Displacement refers to either vertical displacement for GPS data or line-of-sight displacement for InSAR data. The red and black lines are the best-fit models to the InSAR IM2 for SCD and the vertical component of the WLKY station. The blue dashed line is the best-fit function $U = U_f(1 - e^{-t/\tau})$ with U_f the maximum displacement and τ a time constant. The right axis shows the pressure P in the deep magma source. The vertical lines show the change in the deep magma pressure P between a linearly increasing pressure to a constant pressure and (green line for GPS and orange line for InSAR). B. Best-fit magma injection model (red line) to the normalized vertical displacements of the WLKY, LKWY and OFW2 stations. The dashed green line is the adimensional mantle pressure function (P_s), and the green continuous line is the best-fit exponential fit of the form $P_s = P(1 - e^{-t/\tau_m})$. The latter function is used to simulate the magma flow between the caldera and NGB (Figure 10 - Figure 11). The vertical green lines in panels A and B do not agree with each other because in panel A the model is applied only to a single GPS station while in B it is applied to the normalized displacements of the three stations.

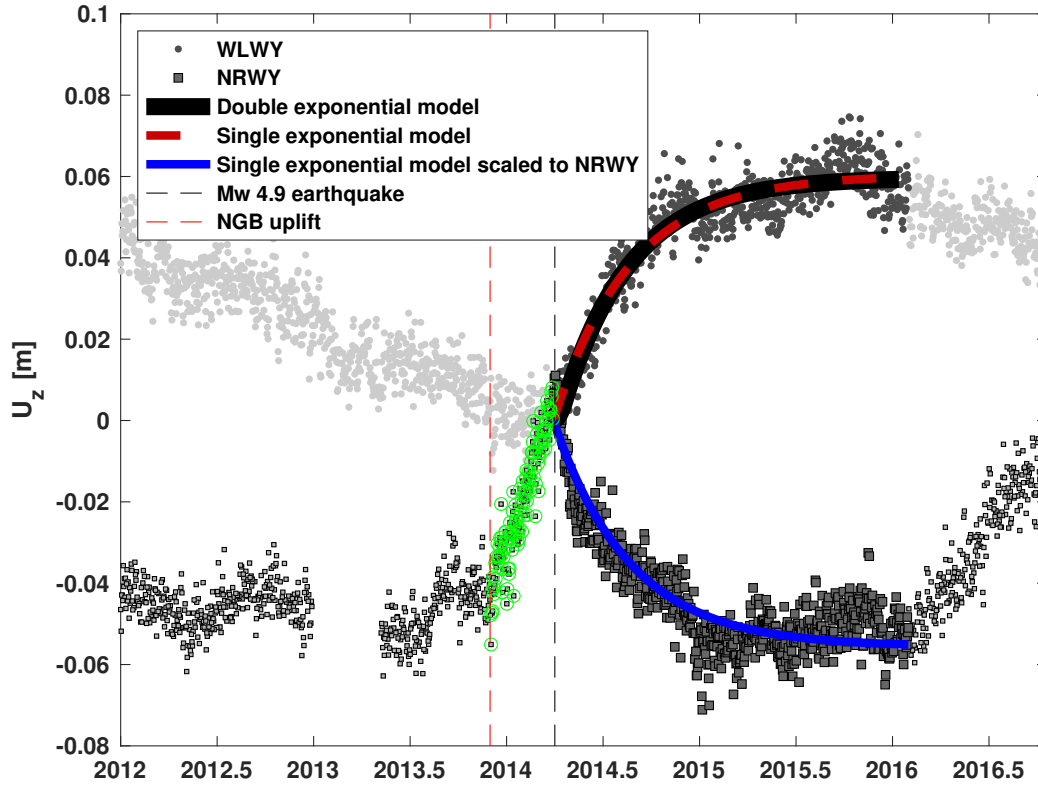


Figure 8: Time series of vertical displacement at stations WLWY and NRWY during 2014-2015, with best-fit models of magma injection for a double exponential (solid black line) and exponential fits of the form $U = U_f(1 - e^{-\frac{t}{\tau}})$ (dashed red line). The green dots show the NGB uplift during December 2013 - March 2014. The blue line is a scaled version of the exponential fit but applied to the NRWY vertical component during the same time span. The dashed vertical line shows the transition from uplift to subsidence at NGB coincident with a [Mw 4.9 earthquake](#) on March 30 2014. The model fit to the time series indicates two things. First, that the GPS data is indicative of magma injection at the caldera sill. Second, the NGB subsidence was coeval and with nearly the same time history as that of the caldera source. This coincidence was not observed during 2004-2009 ([Figure 7](#)).

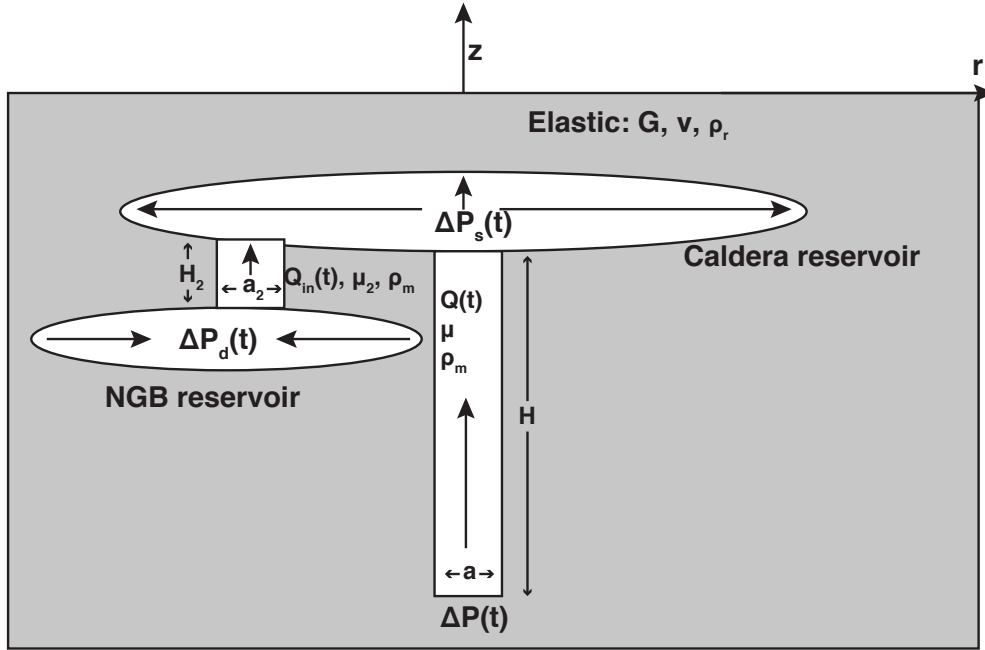


Figure 9: Sketch that shows the main physical parameters involved in the dynamic model of magma injection (Figure 10, Equation 11). The model is made up of two reservoirs that are penny-shaped cracks, but vertically exaggerated in the figure. Here P_s and P_d represent the pressure in the caldera floor and NGB reservoirs which are hydraulically connected. Magma ascends from a mantle source to the caldera source, which is also filled by magma flowing from the NGB source. The model does not consider large areas of partial melt inferred from V_P tomography (Farrell et al., 2014; Huang et al., 2015) and how the melt can either bypass or interact with these areas.

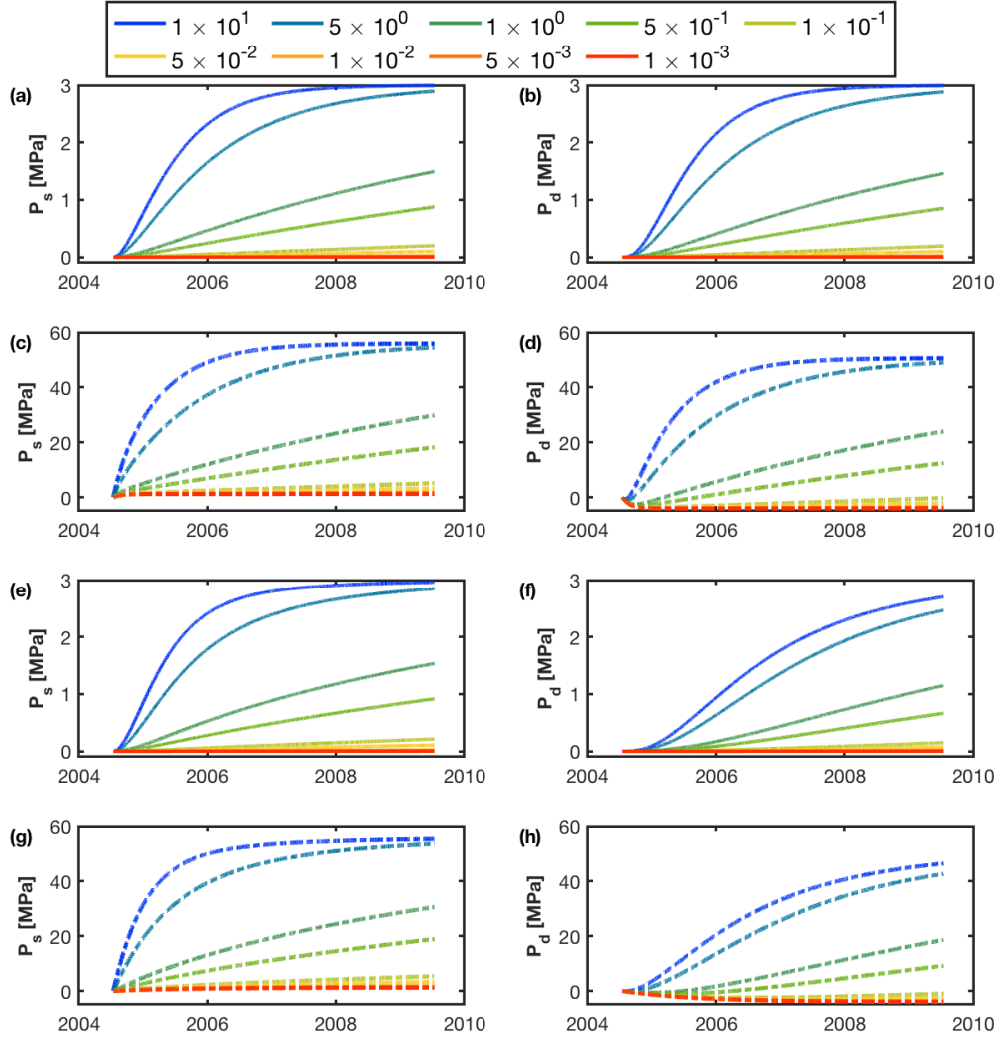


Figure 10: Simulation of the pressure change in the caldera source (P_s , a,c,e,g) and NGB (P_d , b,d,f,h) reservoirs based on the analytic model of magma transfer between the caldera floor and NGB (Equation 11) for the 2004-2009 time period. Panels a-b show simulations with conduit flow due to magma overpressure while panels c-d show models with flow due to both magma overpressure and buoyancy. The colored lines show simulations for different conduit conductivities between the caldera sources and a deep mantle source. a-d) and e-h) show simulations for conduit conductivities of 1 and 0.1 between the caldera sill and the deeper NGB sill. Deformation due to magma injection is proportional to the source pressure change in a linear elastic half-space, so the ground deformation follows functions with the same shape as the source pressure function. The models show that magma extraction from NGB to the caldera floor cannot explain both the deformation trends observed in the GPS (Figure 1) and InSAR (Figure 3) data.

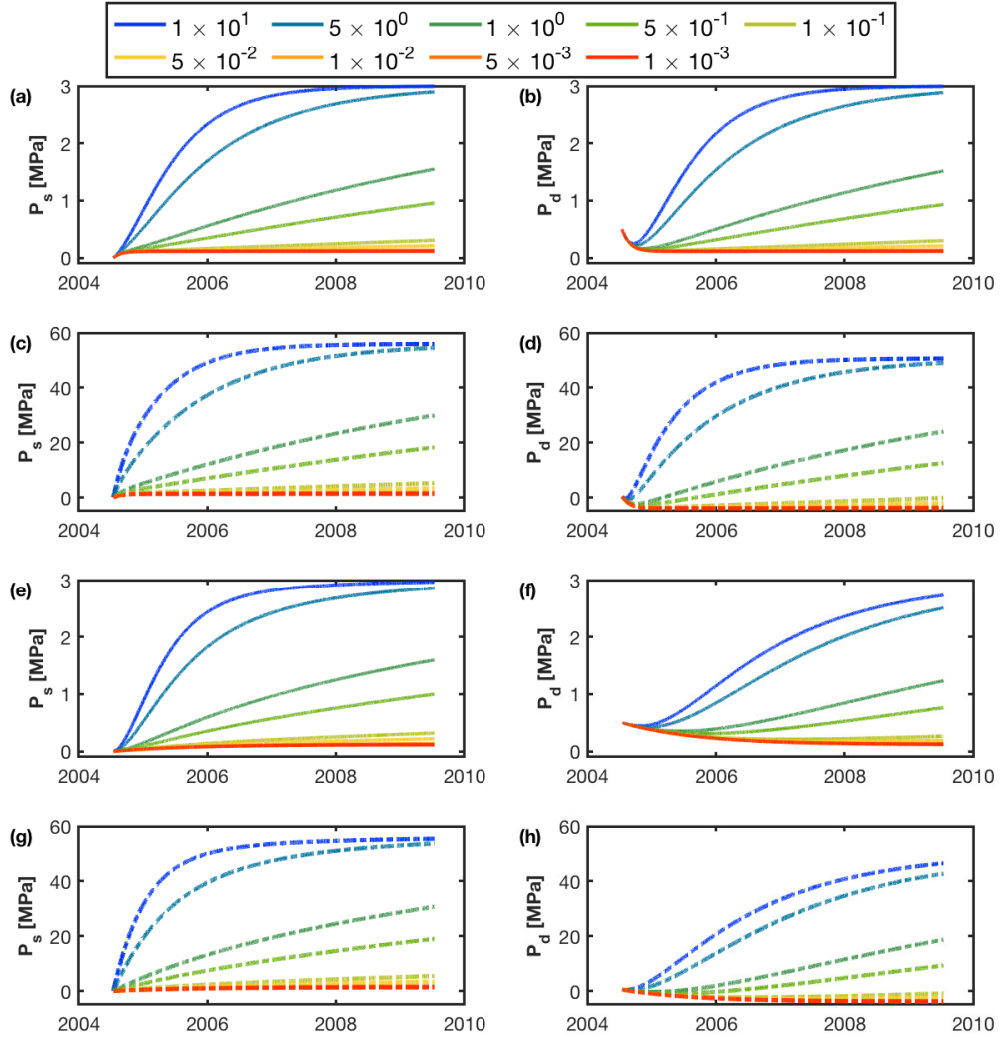


Figure 11: Same as Figure 10 but with $P_{d0} = 0.5$ MPa for the NGB sill. This simulation shows that magma extraction from NGB to the caldera can produce subsidence at NGB with a similar amplitude to that of the caldera uplift only if the NGB sill overpressure is unrealistically higher than the overpressure at the caldera sill.

References

974

975

976

977

978

979

980

981

982

983

984

985

986

987

988

989

990

991

992

993

994

995

996

997

998

999

1000

1001

1002

1003

1004

1005

1006

1007

1008

1009

1010

1011

1012

1013

1014

1015

1016

1017

1018

1019

1020

1021

1022

1023

1024

1025

- Acocella, V. (2019), Bridging the gap from caldera unrest to resurgence, *Frontiers in Earth Science*, 10.3389/feart.2019.00173.
- Albino, F., and F. Sigmundsson (2014), Stress transfer between magma bodies: Influence of intrusions prior to 2010 eruptions at Eyjafjallajökull volcano, Iceland, *Journal of Geophysical Research-Solid Earth*, 119(4), 2964–2975, 10.1002/2013jb010510.
- Albino, F., V. Pinel, and F. Sigmundsson (2010), Influence of surface load variations on eruption likelihood: application to two Icelandic subglacial volcanoes, Grimsvotn and Katla, *Geophysical Journal International*, 181(3), 1510–1524, 10.1111/j.1365-246X.2010.04603.x.
- Aly, M. H., and E. S. Cochran (2011), Spatio-temporal evolution of Yellowstone deformation between 1992 and 2009 from InSAR and GPS observations, *Bulletin of Volcanology*, 10.1007/s00445-011-0483-y.
- Amoruso, A., and L. Crescentini (2009), Shape and volume change of pressurized ellipsoidal cavities from deformation and seismic data, *Journal of Geophysical Research-Solid Earth*, 114, 10.1029/2008jb005946.
- Anderson, K., and P. Segall (2013), Bayesian inversion of data from effusive volcanic eruptions using physics-based models: Application to Mount St. Helens 2004-2008, *Journal of Geophysical Research-Solid Earth*, 118(5), 2017–2037, 10.1002/jgrb.50169.
- Annen, C. (2009), From plutons to magma chambers: Thermal constraints on the accumulation of eruptible silicic magma in the upper crust, *Earth and Planetary Science Letters*, 284(3-4), 409–416, 10.1016/j.epsl.2009.05.006.
- Annen, C., J. D. Blundy, J. Leuthold, and R. S. J. Sparks (2015), Construction and evolution of igneous bodies: Towards an integrated perspective of crustal magmatism, *Lithos*, 230, 206–221, 10.1016/J.LITHOS.2015.05.008.
- Aster, R. C., B. Borchers, and C. H. Thurber (2018), *Parameter estimation and inverse problems*, Elsevier, 10.1016/C2015-0-02458-3.
- Bachmann, O., and G. Bergantz (2008), The magma reservoirs that feed supereruptions, *Elements*, 4(1), 17–21, 10.2113/gselements.4.1.17.
- Bachmann, O., and C. Huber (2016), Silicic magma reservoirs in the Earth’s crust, *American Mineralogist*, 101(11), 2377–2404, 10.2138/am-2016-5675.
- Bagnardi, M., F. Amelung, and M. P. Poland (2013), A new model for the growth of basaltic shields based on deformation of Fernandina volcano, Galápagos Islands, *Earth and Planetary Science Letters*, 10.1016/j.epsl.2013.07.016.
- Berardino, P., G. Fornaro, R. Lanari, and E. Sansosti (2002), A new algorithm for surface deformation monitoring based on small baseline differential SAR interferograms, *Ieee Transactions on Geoscience and Remote Sensing*, 40(11), 2375–2383, 10.1109/tgrs.2002.803792.
- Biggs, J., and C. Annen (2019), The lateral growth and coalescence of magma systems, *Philosophical Transactions of the Royal Society A: Mathematical, Physical and Engineering Sciences*, 377(2139), 20180,005, 10.1098/rsta.2018.0005.
- Blewitt, G., W. Hammond, and C. Kreemer (2018), Harnessing the GPS Data Explosion for Interdisciplinary Science, *Eos*, 10.1029/2018eo104623.
- Carrier, A., J. L. Got, A. Peltier, V. Ferrazzini, T. Staudacher, P. Kowalski, and P. Boissier (2015), A damage model for volcanic edifices: Implications for edifice strength, magma pressure, and eruptive processes, *Journal of Geophysical Research: Solid Earth*, 10.1002/2014JB011485.
- Cashman, K. V., R. S. J. Sparks, and J. D. Blundy (2017), Vertically extensive and unstable magmatic systems: A unified view of igneous processes, *Science*, 10.1126/science.aag3055.

- 1026 Cayol, V., and F. H. Cornet (1997), 3D mixed boundary elements for elastostatic
 1027 deformation field analysis, *International journal of rock mechanics and mining*
 1028 *sciences & geomechanics abstracts*, 10.1016/S0148-9062(96)00035-6.
- 1029 Chang, W.-L., R. B. Smith, C. Wicks, J. M. Farrell, and C. M. Puskas (2007), Ac-
 1030 celerated uplift and magmatic intrusion of the Yellowstone caldera, 2004 to 2006,
 1031 *Science*, 318(5852), 952–956, 10.1126/science.1146842.
- 1032 Chang, W.-L., R. B. Smith, J. Farrell, and C. M. Puskas (2010), An extraordinary
 1033 episode of Yellowstone caldera uplift, 2004-2010, from GPS and InSAR observa-
 1034 tions, *Geophysical Research Letters*, 37, 10.1029/2010gl045451.
- 1035 Chen, C. W., and H. A. Zebker (2001), Two-dimensional phase unwrapping with use
 1036 of statistical models for cost functions in nonlinear optimization, *Journal of the*
 1037 *Optical Society of America a-Optics Image Science and Vision*, 18(2), 338–351,
 1038 10.1364/josaa.18.000338.
- 1039 Christiansen, R. L. (2001), The Quaternary and Pliocene Yellowstone Plateau vol-
 1040 canic field of Wyoming, Idaho, and Montana, *US Geological Survey Professional*
 1041 *Paper*, 10.3133/pp729G.
- 1042 Cooper, K. M. (2017), What Does a Magma Reservoir Look Like? The "Crystal's-
 1043 Eye" View, *Elements*, 13(1), 23–28, 10.2113/gselements.13.1.23.
- 1044 Cooper, K. M., and A. J. Kent (2014), Rapid remobilization of magmatic crystals
 1045 kept in cold storage, *Nature*, 10.1038/nature12991.
- 1046 D'Auria, L., S. Pepe, R. Castaldo, F. Giudicepietro, G. Macedonio, P. Ricciolino,
 1047 P. Tizzani, F. Casu, R. Lanari, M. Manzo, M. Martini, E. Sansosti, and I. Zinno
 1048 (2015), Magma injection beneath the urban area of Naples: A new mechanism
 1049 for the 2012-2013 volcanic unrest at Campi Flegrei caldera, *Scientific Reports*,
 1050 10.1038/srep13100.
- 1051 Davidge, L., C. Ebinger, M. Ruiz, G. Tepp, F. Amelung, D. Geist, D. Coté, and
 1052 J. Anzieta (2017), Seismicity patterns during a period of inflation at Sierra Negra
 1053 volcano, Galápagos Ocean Island Chain, *Earth and Planetary Science Letters*,
 1054 10.1016/j.epsl.2016.12.021.
- 1055 de Zeeuw-van Dalssen, E., H. Rymer, E. Sturkell, R. Pedersen, A. Hooper, F. Sig-
 1056 mundsson, and B. Ófeigsson (2013), Geodetic data shed light on ongoing caldera
 1057 subsidence at Askja, Iceland, *Bulletin of Volcanology*, 10.1007/s00445-013-0709-2.
- 1058 Degruyter, W., and C. Huber (2014), A model for eruption frequency of upper
 1059 crustal silicic magma chambers, *Earth and Planetary Science Letters*, 403, 117–
 1060 130, 10.1016/j.epsl.2014.06.047.
- 1061 Delgado, F. (2020), Rhyolitic volcano dynamics in the Southern Andes: Contribu-
 1062 tions from 17 years of InSAR observations at Cordón Caulle from 2003 to 2020,
 1063 *Journal of South American Earth Sciences*, 10.1016/j.jsames.2020.102841.
- 1064 Delgado, F., M. E. Pritchard, D. Basualto, J. Lazo, L. Cordova, and L. E. Lara
 1065 (2016), Rapid reinflation following the 2011-2012 rhyodacite eruption at Cordon
 1066 Caulle volcano (Southern Andes) imaged by InSAR: Evidence for magma reservoir
 1067 refill, *Geophysical Research Letters*, 43(18), 9552–9562, 10.1002/2016gl070066.
- 1068 Delgado, F., M. Pritchard, S. Samsonov, and L. Córdova (2018), Renewed post-
 1069 eruptive uplift following the 2011-2012 rhyolitic eruption of Cordón Caulle
 1070 (Southern Andes, Chile): evidence for transient episodes of magma reser-
 1071 voir recharge during 2012-2018, *Journal of Geophysical Research: Solid Earth*,
 1072 10.1029/2018JB016240.
- 1073 Delgado, F., J. Kubanek, K. Anderson, P. Lundgren, and M. Pritchard (2019),
 1074 Physicochemical models of effusive rhyolitic eruptions constrained with InSAR
 1075 and DEM data: A case study of the 2011-2012 Cordón Caulle eruption, *Earth and*
 1076 *Planetary Science Letters*, 524, 115,736, 10.1016/J.EPSL.2019.115736.
- 1077 Doin, M. P., C. Lasserre, G. Peltzer, O. Cavalie, and C. Doubre (2009), Cor-
 1078 rections of stratified tropospheric delays in SAR interferometry: Validation
 1079 with global atmospheric models, *Journal of Applied Geophysics*, 69(1), 35–50,

- 1080 10.1016/j.jappgeo.2009.03.010.
- 1081 Doin, M.-P., F. Lodge, S. Guillaso, R. Jolivet, C. Lasserre, G. Ducret, R. Grandin,
1082 E. Pathier, and V. Pinel (2011), Presentation of the small baseline NSBAS pro-
1083 cessing chain on a case example: the Etna deformation monitoring from 2003 to
1084 2010 using Envisat data, in *Proceedings of the ESA Fringe Workshop*.
- 1085 Druitt, T. H., D. M. Pyle, and T. A. Mather (2019), Santorini volcano and its
1086 plumbing system, *Elements*, 10.2138/gselements.15.3.177.
- 1087 Ducret, G., M.-P. Doin, R. Grandin, C. Lasserre, and S. Guillaso (2014), DEM
1088 Corrections Before Unwrapping in a Small Baseline Strategy for InSAR Time
1089 Series Analysis, *Ieee Geoscience and Remote Sensing Letters*, 11(3), 696–700,
1090 10.1109/lgrs.2013.2276040.
- 1091 Dvorak, J. J., and G. Berrino (1991), Recent ground movement and seismic ac-
1092 tivity in Campi Flegrei, southern Italy: episodic growth of a resurgent dome,
1093 *Journal of Geophysical Research-Solid Earth and Planets*, 96(B2), 2309–2323,
1094 10.1029/90jb02225.
- 1095 Dzurisin, D., and Z. Lu (2007), Interferometric synthetic-aperture radar (InSAR),
1096 in *Volcano Deformation*, edited by D. Dzurisin, chap. 5, pp. 153–194, Springer,
1097 Berlin, Heidelberg, 10.1007/978-3-540-49302-0_5.
- 1098 Dzurisin, D., J. C. Savage, and R. O. Fournier (1990), Recent crustal subsidence at
1099 Yellowstone Caldera, Wyoming, *Bulletin of Volcanology*, 10.1007/BF00304098.
- 1100 Dzurisin, D., C. Wicks, and W. Thatcher (1999), Renewed uplift at the Yellowstone
1101 caldera measured by leveling surveys and satellite radar interferometry, *Bulletin of*
1102 *Volcanology*, 10.1007/s004450050277.
- 1103 Dzurisin, D., C. W. Wicks, and M. P. Poland (2012), History of surface displace-
1104 ments at the Yellowstone Caldera, Wyoming, from leveling surveys and InSAR
1105 observations, 19232008, *U.S. Geological Survey Professional Paper*, 1788, 68 p.
- 1106 Dzurisin, D., Z. Lu, M. P. Poland, and C. W. Wicks (2019), Space-Based Imag-
1107 ing Radar Studies of U.S. Volcanoes, *Frontiers in Earth Science*, 6, 249,
1108 10.3389/feart.2018.00249.
- 1109 Evans, W. C., D. Bergfeld, M. C. van Soest, M. A. Huebner, J. Fitzpatrick, and
1110 K. M. Revesz (2006), Geochemistry of low-temperature springs northwest of Yel-
1111 lowstone caldera: Seeking the link between seismicity, deformation, and fluid flow,
1112 *Journal of Volcanology and Geothermal Research*, 10.1016/j.jvolgeores.2006.01.001.
- 1113 Farrell, J. (2014), Seismicity and tomographic imaging of the Yellowstone crustal
1114 magmatic-tectonic system, Ph.D. thesis, University of Utah.
- 1115 Farrell, J., S. Husen, and R. B. Smith (2009), Earthquake swarm and b-value char-
1116 acterization of the Yellowstone volcano-tectonic system, *Journal of Volcanology*
1117 *and Geothermal Research*, 10.1016/j.jvolgeores.2009.08.008.
- 1118 Farrell, J., R. B. Smith, T. Taira, W.-L. Chang, and C. M. Puskas (2010), Dynam-
1119 ics and rapid migration of the energetic 2008-2009 Yellowstone Lake earthquake
1120 swarm, *Geophysical Research Letters*, 37(19), n/a–n/a, 10.1029/2010GL044605.
- 1121 Farrell, J., R. B. Smith, S. Husen, and T. Diehl (2014), Tomography from 26 years
1122 of seismicity revealing that the spatial extent of the Yellowstone crustal magma
1123 reservoir extends well beyond the Yellowstone caldera, *Geophysical Research Let-*
1124 *ters*, 10.1002/2014GL059588.
- 1125 Feigl, K. L., H. Le Mével, S. T. Ali, L. Cordova, N. L. Andersen, C. DeMets, and
1126 B. S. Singer (2014), Rapid uplift in Laguna del Maule volcanic field of the Andean
1127 Southern Volcanic zone (Chile) 2007-2012, *Geophysical Journal International*,
1128 196(2), 885–901, 10.1093/gji/ggt438.
- 1129 Fialko, Y. (2004a), Evidence of fluid-filled upper crust from observations of postseis-
1130 mic deformation due to the 1992 Mw7.3 Landers earthquake, *Journal of Geophysi-*
1131 *cal Research: Solid Earth*, 10.1029/2004JB002985.
- 1132 Fialko, Y. (2004b), Probing the mechanical properties of seismically active
1133 crust with space geodesy: Study of the coseismic deformation due to the 1992

- 1134 *M* _{*w*} 7.3 Landers (southern California)
 1135 earthquake, *Journal of Geophysical Research*, 109(B3), B03,307, 10.1029/
 1136 2003JB002756.
- 1137 Fialko, Y., M. Simons, and Y. Khazan (2001a), Finite source modelling of magmatic
 1138 unrest in Socorro, New Mexico, and Long Valley, California, *Geophysical Journal
 1139 International*, 10.1046/j.1365-246X.2001.00453.x.
- 1140 Fialko, Y., Y. Khazan, and M. Simons (2001b), Deformation due to a pressur-
 1141 ized horizontal circular crack in an elastic half-space, with applications to vol-
 1142 cano geodesy, *Geophysical Journal International*, 146(1), 181–190, 10.1046/
 1143 j.1365-246X.2001.00452.x.
- 1144 Fournier, R. O. (1989), Geochemistry and dynamics of the Yellowstone National
 1145 Park hydrothermal system, *Annual review of earth and planetary sciences. Vol.
 1146 17*, 10.1146/annurev.earth.17.1.13.
- 1147 Fournier, R. O. (2007), Hydrothermal systems and volcano geochemistry, in *Vol-
 1148 cano Deformation*, edited by D. Dzurisin, chap. 10, pp. 323–341, Springer, Berlin,
 1149 Heidelberg, 10.1007/978-3-540-49302-0_10.
- 1150 Fukushima, Y., V. Cayol, P. Durand, and D. Massonnet (2010), Evolution of magma
 1151 conduits during the 1998-2000 eruptions of Piton de la Fournaise volcano, Reunion
 1152 Island, *Journal of Geophysical Research-Solid Earth*, 115, 10.1029/2009jb007023.
- 1153 Gerbault, M. (2012), Pressure conditions for shear and tensile failure around a cir-
 1154 cular magma chamber; insight from elasto-plastic modelling, *Geological Society,
 1155 London, Special Publications*, 367, 111-130, 10.1144/SP367.8.
- 1156 Giordano, D., and D. B. Dingwell (2003), Non-Arrhenian multicomponent melt vis-
 1157 cosity: A model, *Earth and Planetary Science Letters*, 10.1016/S0012-821X(03)
 1158 00042-6.
- 1159 Giudicepietro, F., G. Macedonio, and M. Martini (2017), A Physical Model of Sill
 1160 Expansion to Explain the Dynamics of Unrest at Calderas with Application to
 1161 Campi Flegrei, *Frontiers in Earth Science*, 5(54), 10.3389/feart.2017.00054.
- 1162 Goldstein, R. M., H. A. Zebker, and C. L. Werner (1988), Satellite radar inter-
 1163 ferometry - two-dimensional phase unwrapping, *Radio Science*, 23(4), 713–720,
 1164 10.1029/RS023i004p00713.
- 1165 Heap, M. J., M. Villeneuve, F. Albino, J. I. Farquharson, E. Brothelande,
 1166 F. Amelung, J. L. Got, and P. Baud (2020), Towards more realistic values of
 1167 elastic moduli for volcano modelling, *Journal of Volcanology and Geothermal
 1168 Research*, 10.1016/j.jvolgeores.2019.106684.
- 1169 Heimisson, E. R., P. Einarsson, F. Sigmundsson, and B. Brandsdottir (2015),
 1170 Kilometer-scale Kaiser effect identified in Krafla volcano, Iceland, *Geophysical
 1171 Research Letters*, 42(19), 7958–7965, 10.1002/2015gl065680.
- 1172 Henderson, S. T., F. Delgado, J. Elliott, M. E. Pritchard, and P. R. Lund-
 1173 gren (2017), Decelerating uplift at Lazufre volcanic center, Central Andes,
 1174 from A.D. 2010 to 2016, and implications for geodetic models, *Geosphere*,
 1175 10.1130/GES01441.1.
- 1176 Hildreth, W. (2017), Fluid-driven uplift at Long Valley Caldera, California: Geo-
 1177 logic perspectives, *Journal of Volcanology and Geothermal Research*, 341, 269–286,
 1178 10.1016/j.jvolgeores.2017.06.010.
- 1179 Hill, D., E. Montgomery-Brown, D. R. Shelly, A. Flinders, and S. Prejean (2020),
 1180 Post-1978 Tumescence at Long Valley Caldera, California: a Geophysical Perspec-
 1181 tive, *Journal of Volcanology and Geothermal Research*, 10.1016/j.jvolgeores.2020
 1182 .106900.
- 1183 Huang, H. H., F. C. Lin, B. Schmandt, J. Farrell, R. B. Smith, and V. C. Tsai
 1184 (2015), The Yellowstone magmatic system from the mantle plume to the upper
 1185 crust, *Science*, 10.1126/science.aaa5648.
- 1186 Huber, C., O. Bachmann, and J. Dufek (2010), The limitations of melting on the
 1187 reactivation of silicic mushes, *Journal of Volcanology and Geothermal Research*,

- 1188 10.1016/j.jvolgeores.2010.06.006.
- 1189 Huber, C., O. Bachmann, and J. Dufek (2011), Thermo-mechanical reactivation of
1190 locked crystal mushes: Melting-induced internal fracturing and assimilation pro-
1191 cesses in magmas, *Earth and Planetary Science Letters*, 10.1016/j.epsl.2011.02.022.
- 1192 Huber, C., O. Bachmann, and J. Dufek (2012), Crystal-poor versus crystal-
1193 rich ignimbrites: A competition between stirring and reactivation, *Geology*,
1194 10.1130/G32425.1.
- 1195 Hutnak, M., S. Hurwitz, S. E. Ingebritsen, and P.A. Hsieh (2009), Numerical models
1196 of caldera deformation: Effects of multiphase and multicomponent hydrothermal
1197 fluid flow, *Journal of Geophysical Research*, 114(B04411), 10.1029/2008JB006151.
- 1198 Hurwitz, S., and J. B. Lowenstern (2014), Dynamics of the Yellowstone hydrother-
1199 mal system, *Reviews of Geophysics*, 52(3), 375–411, 10.1002/2014rg000452.
- 1200 Hurwitz, S., and M. Manga (2017), The Fascinating and Complex Dynam-
1201 ics of Geyser Eruptions, *Annual Review of Earth and Planetary Sciences*,
1202 10.1146/annurev-earth-063016-015605.
- 1203 Hurwitz, S., L. B. Christiansen, and P. A. Hsieh (2007a), Hydrothermal fluid flow
1204 and deformation in large calderas: Inferences from numerical simulations, *Journal*
1205 *of Geophysical Research-Solid Earth*, 112(B2), 10.1029/2006jb004689.
- 1206 Hurwitz, S., J. B. Lowenstern, and H. Heasler (2007b), Spatial and temporal geo-
1207 chemical trends in the hydrothermal system of Yellowstone National Park: Infer-
1208 ences from river solute fluxes, *Journal of Volcanology and Geothermal Research*,
1209 10.1016/j.jvolgeores.2007.01.003.
- 1210 Hurwitz, S., W. C. Evans, and J. B. Lowenstern (2010), River solute fluxes reflect-
1211 ing active hydrothermal chemical weathering of the Yellowstone Plateau Volcanic
1212 Field, USA, *Chemical Geology*, 10.1016/j.chemgeo.2010.07.001.
- 1213 Hurwitz, S., A. G. Hunt, and W. C. Evans (2012), Temporal variations of geyser
1214 water chemistry in the Upper Geyser Basin, Yellowstone National Park, USA,
1215 *Geochemistry, Geophysics, Geosystems*, 10.1029/2012GC004388.
- 1216 Jaupart, C., and S. Tait (1990), Dynamics of eruptive phenomena, *Reviews in Min-
1217 eralogy*, 24, 213–238.
- 1218 Jay, J., F. Costa, M. Pritchard, L. Lara, B. Singer, and J. Herrin (2014), Locating
1219 magma reservoirs using InSAR and petrology before and during the 2011-2012
1220 Cordon Caulle silicic eruption, *Earth and Planetary Science Letters*, 403, 463,
1221 10.1016/j.epsl.2014.07.021.
- 1222 Jellinek, A. M., and D. J. DePaolo (2003), A model for the origin of large silicic
1223 magma chambers: precursors of caldera-forming eruptions, *Bulletin of Volcanol-
1224 ogy*, 65(5), 363–381, 10.1007/s00445-003-0277-y.
- 1225 Jolivet, R., R. Grandin, C. Lasserre, M. P. Doin, and G. Peltzer (2011), Systematic
1226 InSAR tropospheric phase delay corrections from global meteorological reanalysis
1227 data, *Geophysical Research Letters*, 38, 10.1029/2011gl048757.
- 1228 Jolivet, R., P. S. Agram, N. Y. Lin, M. Simons, M.-P. Doin, G. Peltzer, and Z. H. Li
1229 (2014), Improving InSAR geodesy using Global Atmospheric Models, *Journal of*
1230 *Geophysical Research-Solid Earth*, 119(3), 2324–2341, 10.1002/2013jb010588.
- 1231 Le Mével, H., K. L. Feigl, L. Córdova, C. DeMets, and P. Lundgren (2015), Evolu-
1232 tion of unrest at Laguna del Maule volcanic field (Chile) from InSAR and GPS
1233 measurements, 2003 to 2014, *Geophysical Research Letters*, 42(16), 6590–6598,
1234 10.1002/2015GL064665.
- 1235 Le Mével, H., P. Gregg, and K. L. Feigl (2016), Magma injection into a long-lived
1236 reservoir to explain geodetically measured uplift: application to the 20072014
1237 unrest episode at Laguna del Maule volcanic field, Chile, *Journal of Geophysical*
1238 *Research: Solid Earth*, pp. n/a–n/a, 10.1002/2016JB013066.
- 1239 Lengline, O., D. Marsan, J. L. Got, V. Pinel, V. Ferrazzini, and P. G. Okubo
1240 (2008), Seismicity and deformation induced by magma accumulation at three
1241 basaltic volcanoes, *Journal of Geophysical Research-Solid Earth*, 113(B12), 12,

- 1242 10.1029/2008jb005937.
- 1243 Lewicki, J. L., P. J. Kelly, D. Bergfeld, R. G. Vaughan, and J. B. Lowenstern (2017),
 1244 Monitoring gas and heat emissions at Norris Geysers Basin, Yellowstone National
 1245 Park, USA based on a combined eddy covariance and Multi-GAS approach, *Jour-
 1246 nal of Volcanology and Geothermal Research*, 10.1016/j.jvolgeores.2017.10.001.
- 1247 Liu, Z., D. Dong, and P. Lundgren (2011), Constraints on time-dependent vol-
 1248 canic source models at Long Valley Caldera from 1996 to 2009 using InSAR and
 1249 geodetic measurements, *Geophysical Journal International*, 187(3), 1283–1300,
 1250 10.1111/j.1365-246X.2011.05214.x.
- 1251 Lohman, R. B., and M. Simons (2005), Some thoughts on the use of InSAR data to
 1252 constrain models of surface deformation: Noise structure and data downsampling,
 1253 *Geochemistry Geophysics Geosystems*, 6, 12, 10.1029/2004gc000841.
- 1254 Lowenstern, J. B., and S. Hurwitz (2008), Monitoring a supervolcano in re-
 1255 pose: Heat and volatile flux at the Yellowstone caldera, *Elements*, 10.2113/
 1256 GSELEMENTS.4.1.35.
- 1257 Lowenstern, J. B., D. Bergfeld, W. C. Evans, and A. G. Hunt (2015), Origins of
 1258 geothermal gases at Yellowstone, 10.1016/j.jvolgeores.2015.06.010.
- 1259 Lowenstern, J. B., T. W. Sisson, and S. Hurwitz (2017), Probing magma reservoirs
 1260 to improve volcano forecasts, *EOS*, 98, doi.org/10.1029/2017EO085189.
- 1261 Lu, Z., and D. Dzurisin (2010), Ground surface deformation patterns, magma sup-
 1262 ply, and magma storage at Okmok volcano, Alaska, from InSAR analysis: 2.
 1263 Coeruptive deflation, July-August 2008, *Journal of Geophysical Research-Solid
 1264 Earth*, 115, 10.1029/2009jb006970.
- 1265 Lu, Z., T. Masterlark, D. Dzurisin, R. Rykhus, and C. Wicks (2003), Magma supply
 1266 dynamics at Westdahl volcano, Alaska, modeled from satellite radar interferome-
 1267 try, *Journal of Geophysical Research-Solid Earth*, 108(B7), 10.1029/2002jb002311.
- 1268 Lu, Z., D. Dzurisin, J. Biggs, C. Wicks, and S. McNutt (2010), Ground surface
 1269 deformation patterns, magma supply, and magma storage at Okmok volcano,
 1270 Alaska, from InSAR analysis: 1. Intereruption deformation, 1997-2008, *Journal of
 1271 Geophysical Research-Solid Earth*, 115, 10.1029/2009jb006969.
- 1272 Lundgren, P., S. Usai, E. Sansosti, R. Lanari, M. Tesauro, G. Fornaro, and P. Ber-
 1273 rardino (2001), Modeling surface deformation observed with synthetic aperture
 1274 radar interferometry at Campi Flegrei caldera, *Journal of Geophysical Research:
 1275 Solid Earth*, 106(B9), 19,355–19,366, 10.1029/2001JB000194.
- 1276 Manga, M., I. Beresnev, E. E. Brodsky, J. E. Elkhoury, D. Elsworth, S. E. Ingebrit-
 1277 sen, D. C. Mays, and C. Y. Wang (2012), Changes in permeability caused by
 1278 transient stresses: Field observations, experiments, and mechanisms, *Reviews of
 1279 Geophysics*, 10.1029/2011RG000382.
- 1280 McTigue, D. F. (1987), Elastic stress and deformation near a finite spherical magma
 1281 body: Resolution of the point source paradox, *Journal of Geophysical Research:
 1282 Solid Earth*, 92(B12), 12,931–12,940, 10.1029/JB092iB12p12931.
- 1283 Miller, C. A., H. Le Mevel, G. Currenti, G. Williams-Jones, and B. Tikoff (2017),
 1284 Microgravity changes at the Laguna del Maule volcanic field: Magma-induced
 1285 stress changes facilitate mass addition, *Journal of Geophysical Research-Solid
 1286 Earth*, 122(4), 3179–3196, 10.1002/2017jb014048.
- 1287 Miller, C. F., and D. A. Wark (2008), Supervolcanoes and their explosive supererup-
 1288 tions, *Elements*, 4(1), 11–15, 10.2113/gselements.4.1.11.
- 1289 Montgomery-Brown, E. K., C. W. Wicks, P. F. Cervelli, J. O. Langbein, J. L. Svarc,
 1290 D. R. Shelly, D. P. Hill, and M. Lisowski (2015), Renewed inflation of Long Valley
 1291 Caldera, California (2011 to 2014), *Geophysical Research Letters*, 42(13), 5250–
 1292 5257, 10.1002/2015gl064338.
- 1293 Newman, A. V., T.H. Dixon, and N. Gourmelen (2006), A four-dimensional vis-
 1294 coelastic deformation model for Long Valley Caldera, California, between 1995
 1295 and 2000, *Journal of Volcanology and Geothermal Research*, 150(1-3), 244–269,

- 1296 10.1016/j.jvolgeores.2005.07.017
- 1297 Novoa, C., D. Remy, M. Gerbault, J.C. Baez, A. Tassara, L. Cordova, C. Cardona,
- 1298 M. Granger, S. Bonvalot, and F. Delgado (2019), Viscoelastic relaxation: A mech-
- 1299 anism to explain the decennial large surface displacements at the Laguna del
- 1300 Maule silicic volcanic complex, *Earth and Planetary Science Letters*, *521*, 49–59,
- 1301 10.1016/j.epsl.2019.06.005.
- 1302 Okada, Y. (1985), Surface deformation due to shear and tensile faults in a half-
- 1303 space, *Bulletin of the Seismological Society of America*, *75*(4), 1135–1154.
- 1304 Parks, M. M., J. Biggs, P. England, T. A. Mather, P. Nomikou, K. Palamartchouk,
- 1305 X. Papanikolaou, D. Paradissis, B. E. Parsons, D. M. Pyle, C. Raptakis, and
- 1306 V. Zacharis (2012), Evolution of Santorini Volcano dominated by episodic
- 1307 and rapid fluxes of melt from depth, *Nature Geoscience*, *5*(10), 749–754,
- 1308 10.1038/ngeo1562.
- 1309 Pascal, K., J. Neuberg, and E. Rivalta (2014), On precisely modelling surface de-
- 1310 formation due to interacting magma chambers and dykes, *Geophysical Journal*
- 1311 *International*, *196*(1), 253–278, 10.1093/gji/ggt343.
- 1312 Pedersen, R., and F. Sigmundsson (2006), Temporal development of the 1999 intru-
- 1313 sive episode in the Eyjafjallajökull volcano, Iceland, derived from InSAR images,
- 1314 *Bulletin of Volcanology*, *68*(4), 377–393, 10.1007/s00445-005-0020-y.
- 1315 Pelton, J. R., and R. B. Smith (1979), Recent crustal uplift in Yellowstone National
- 1316 Park, *Science*, 10.1126/science.206.4423.1179.
- 1317 Pierce, K. L., K. P. Cannon, G. A. Meyer, M. J. Trebesch, and R. D. Watts (2002),
- 1318 Post-Glacial Inflation-Deflation Cycles, Tilting, and Faulting in the Yellowstone
- 1319 Caldera Based on Yellowstone Lake Shorelines Open-File Report 02-0142, *US*
- 1320 *Geological Survey Professional Paper*.
- 1321 Pinel, V., and C. Jaupart (2003), Magma chamber behavior beneath a volcanic edi-
- 1322 fice, *Journal of Geophysical Research-Solid Earth*, *108*(B2), 10.1029/2002jb001751.
- 1323 Pinel, V., C. Jaupart, and F. Albino (2010), On the relationship between cycles
- 1324 of eruptive activity and growth of a volcanic edifice, *Journal of Volcanology and*
- 1325 *Geothermal Research*, *194*(4), 150–164, 10.1016/j.jvolgeores.2010.05.006.
- 1326 Poland, M., R. Bürgmann, D. Dzurisin, M. Lisowski, T. Masterlark, S. Owen, and
- 1327 J. Fink (2006), Constraints on the mechanism of long-term, steady subsidence
- 1328 at Medicine Lake volcano, northern California, from GPS, leveling, and InSAR,
- 1329 *Journal of Volcanology and Geothermal Research*, 10.1016/j.jvolgeores.2005.07.007.
- 1330 Poland, M. P., and E. Zeeuwvan Dalfsen (2019), Assessing Seasonal Changes in Mi-
- 1331 crogravity at Yellowstone Caldera, *Journal of Geophysical Research: Solid Earth*,
- 1332 p. 2018JB017061, 10.1029/2018JB017061.
- 1333 Pritchard, M. E., and M. Simons (2004), An InSAR-based survey of volcanic
- 1334 deformation in the southern Andes, *Geophysical Research Letters*, *31*(15), 4,
- 1335 10.1029/2004gl020545.
- 1336 Pritchard, M. E., T. A. Mather, S. R. McNutt, F. J. Delgado, and K. Reath (2019),
- 1337 Thoughts on the criteria to determine the origin of volcanic unrest as magmatic or
- 1338 non-magmatic, *Philosophical Transactions of the Royal Society A: Mathematical,*
- 1339 *Physical and Engineering Sciences*, *377*(2139), 20180,008, 10.1098/rsta.2018.0008.
- 1340 Puskas, C. M., R. B. Smith, C. M. Meertens, and W. L. Chang (2007), Crustal
- 1341 deformation of the Yellowstone-Snake River Plain volcano-tectonic system: Cam-
- 1342 paign and continuous GPS observations, 1987-2004, *Journal of Geophysical Re-*
- 1343 *search: Solid Earth*, 10.1029/2006JB004325.
- 1344 Reverso, T., J. Vandemeulebrouck, F. Jouanne, V. Pinel, T. Villemin, E. Sturkell,
- 1345 and P. Bascou (2014), A two-magma chamber model as a source of deformation at
- 1346 Grimsvotn Volcano, Iceland, *Journal of Geophysical Research-Solid Earth*, *119*(6),
- 1347 4666–4683, 10.1002/2013jb010569.
- 1348 Rivalta, E. (2010), Evidence that coupling to magma chambers controls the volume
- 1349 history and velocity of laterally propagating intrusions, *Journal of Geophysical*

- 1350 *Research: Solid Earth*, 10.1029/2009JB006922.
- 1351 Rosen, P. A., S. Hensley, G. Peltzer, and M. Simons (2004), Updated repeat orbit
1352 interferometry package released, *Eos, Transactions American Geophysical Union*,
1353 85(5), 47, 10.1029/2004EO050004.
- 1354 Rubin, A. E., K. M. Cooper, C. B. Till, A. J. Kent, F. Costa, M. Bose, D. Gravley,
1355 C. Deering, and J. Cole (2017), Rapid cooling and cold storage in a silicic magma
1356 reservoir recorded in individual crystals, *Science*, 10.1126/science.aam8720.
- 1357 Russo, E., G. Waite, and A. Tibaldi (2017), Evaluation of the evolving stress field
1358 of the Yellowstone volcanic plateau, 1988 to 2010, from earthquake first-motion
1359 inversions, *Tectonophysics*, 700-701, 80–91, 10.1016/J.TECTO.2017.02.009.
- 1360 Sambridge, M. (1999), Geophysical inversion with a neighbourhood algorithm - I.
1361 Searching a parameter space, *Geophysical Journal International*, 138(2), 479–494,
1362 10.1046/j.1365-246X.1999.00876.x.
- 1363 Schmandt, B., C. Jiang, and J. Farrell (2019), Seismic perspectives from the
1364 western U.S. on magma reservoirs underlying large silicic calderas, 10.1016/
1365 j.jvolgeores.2019.07.015.
- 1366 Segall, P. (2013), Volcano deformation and eruption forecasting, *Remote Sensing of*
1367 *Volcanoes and Volcanic Processes: Integrating Observation and Modelling*, 380,
1368 85–106, 10.1144/sp380.4.
- 1369 Segall, P. (2019), Magma chambers: What we can, and cannot, learn from volcano
1370 geodesy, 10.1098/rsta.2018.0158.
- 1371 Shelly, D. R., D. P. Hill, F. Massin, J. Farrell, R. B. Smith, and T. Taira (2013), A
1372 fluid-driven earthquake swarm on the margin of the Yellowstone caldera, *Journal*
1373 *of Geophysical Research E: Planets*, 10.1002/jgrb.50362.
- 1374 Sigmundsson, F., S. Hreinsdottir, A. Hooper, T. Arnadottir, R. Pedersen, M. J.
1375 Roberts, N. Oskarsson, A. Auriac, J. Decriem, P. Einarsson, H. Geirsson, M. Hen-
1376 sch, B. G. Ofeigsson, E. Sturkell, H. Sveinbjornsson, and K. L. Feigl (2010), Intru-
1377 sion triggering of the 2010 Eyjafjallajökull explosive eruption, *Nature*, 468(7322),
1378 426–U253, 10.1038/nature09558.
- 1379 Sparks, R. S. J., and K. V. Cashman (2017), Dynamic Magma Systems: Impli-
1380 cations for Forecasting Volcanic Activity, *Elements*, 13(1), 35–40, 10.2113/
1381 gselements.13.1.35.
- 1382 Sparks, R. S. J., C. Annen, J. D. Blundy, K. V. Cashman, A. C. Rust, and M. D.
1383 Jackson (2019), Formation and dynamics of magma reservoirs, *Philosophical*
1384 *Transactions of the Royal Society A: Mathematical, Physical and Engineering*
1385 *Sciences*, 377(2139), 20180,019, 10.1098/rsta.2018.0019.
- 1386 Taira, T., R. B. Smith, and W. L. Chang (2010), Seismic evidence for dilatational
1387 source deformations accompanying the 2004-2008 Yellowstone accelerated uplift
1388 episode, *Journal of Geophysical Research: Solid Earth*, 10.1029/2008JB006281.
- 1389 Tait, S., C. Jaupart, and S. Vergnolle (1989), Pressure, gas content and eruption pe-
1390 riodicity of a shallow, crystallizing magma chamber, *Earth and Planetary Science*
1391 *Letters*, 92(1), 107–123, 10.1016/0012-821x(89)90025-3.
- 1392 Tarantola, A., and B. Valette (1982), Generalized nonlinear inverse problems solved
1393 using the least squares criterion, 10.1029/RG020i002p00219.
- 1394 Tizzani, P., M. Battaglia, R. Castaldo, A. Pepe, G. Zeni, and R. Lanari (2015),
1395 Magma and fluid migration at Yellowstone Caldera in the last three decades in-
1396 ferred from InSAR, leveling, and gravity measurements, *Journal of Geophysical*
1397 *Research-Solid Earth*, 120(4), 2627–2647, 10.1002/2014jb011502.
- 1398 Todesco, M., A.P. Rinaldi, and M. Bonafede, (2010), Modeling of unrest signals
1399 in heterogeneous hydrothermal systems, *Journal of Geophysical Research-Solid*
1400 *Earth*, 115, B09213, 10.1029/2010JB007474.
- 1401 Townsend, M., C. Huber, W. Degruyter, and O. Bachmann (2019), Magma chamber
1402 growth during inter-caldera periods: insights from thermo-mechanical modeling
1403 with applications to Laguna del Maule, Campi Flegrei, Santorini, and Aso, *Geo-*

- 1404 *chemistry, Geophysics, Geosystems*, 10.1029/2018GC008103.
- 1405 Trasatti, E., M. Polcari, M. Bonafede, and S. Stramondo (2015), Geodetic con-
1406 straints to the source mechanism of the 2011-2013 unrest at Campi Flegrei (Italy)
1407 caldera, *Geophysical Research Letters*, 10.1002/2015GL063621.
- 1408 Troise, C., G. De Natale, R. Schiavone, R. Somma, and R. Moretti (2019), The
1409 Campi Flegrei caldera unrest: Discriminating magma intrusions from hydrother-
1410 mal effects and implications for possible evolution, 10.1016/j.earscirev.2018.11.007.
- 1411 Vasco, D. W., C. M. Puskas, R. B. Smith, and C. M. Meertens (2007), Crustal de-
1412 formation and source models of the Yellowstone volcanic field from geodetic data,
1413 *Journal of Geophysical Research: Solid Earth*, 10.1029/2006JB004641.
- 1414 Waite, G. P., and R. B. Smith (2002), Seismic evidence for fluid migration accom-
1415 panying subsidence of the Yellowstone caldera, *Journal of Geophysical Research:*
1416 *Solid Earth*, 10.1029/2001jb000586.
- 1417 Walwer, D., M. Ghil, and E. Calais (2019), Oscillatory nature of the Okmok vol-
1418 cano's deformation, *Earth and Planetary Science Letters*, 10.1016/j.epsl.2018.10
1419 .033.
- 1420 Wdowinski, S., and S. H. Hong (2015), Wetland inSAR: A review of the technique
1421 and applications, in *Remote Sensing of Wetlands: Applications and Advances*,
1422 10.1201/b18210.
- 1423 Wicks, C., W. Thatcher, and D. Dzurisin (1998), Migration of fluids beneath Yel-
1424 lowstone caldera inferred from satellite radar interferometry, *Science*, 282(5388),
1425 458–462, 10.1126/science.282.5388.458.
- 1426 Wicks, C. W., W. Thatcher, D. Dzurisin, and J. Svarc (2006), Uplift, thermal unrest
1427 and magma intrusion at Yellowstone caldera, *Nature*, 10.1038/nature04507.
- 1428 Wicks, C. W., D. Dzurisin, J. B. Lowenstern, and J. Svarc (2020), Magma in-
1429 trusion and volatile ascent beneath Norris Geyser Basin, Yellowstone National
1430 Park, *Journal of Geophysical Research: Solid Earth*, n/a(n/a), e2019JB018,208,
1431 10.1029/2019JB018208.